

# ***Epitaxial YBa<sub>2</sub>Cu<sub>3</sub>O<sub>7-x</sub> nanocomposite thin films from colloidal solutions***

*P Cayado<sup>1</sup>, K De Keukeleere<sup>2</sup>, A Garzón<sup>3</sup>, L Perez-Mirabet<sup>3</sup>, A Meledin<sup>4</sup>, J De Roo<sup>2</sup>, F Vallés<sup>1</sup>, B Mundet<sup>1</sup>, H Rijckaert<sup>2</sup>, G Pollefeyt<sup>2</sup>, M Coll<sup>1</sup>, S Ricart<sup>1</sup>, A Palau<sup>1</sup>, J Gázquez<sup>1</sup>, J Ros<sup>3</sup>, G. Van Tendeloo<sup>4</sup>, I Van Driessche<sup>2</sup>, T Puig<sup>1</sup>, X Obradors<sup>1</sup>*

<sup>1</sup> Institut de Ciència de Materials de Barcelona, ICMAB – CSIC, Campus UA Barcelona, E-08193 Bellaterra, Catalonia, Spain

<sup>2</sup> Sol-Gel Centre for Research on Inorganic Powders and Thin Film Synthesis, SCRiPTS, Dpt. Of Inorganic and Physical Chemistry, Ghent University, Krijgslaan 281 S3, 9000 Ghent, Belgium

<sup>3</sup> Departament de Química, Facultat de Ciències, Universitat Autònoma de Barcelona, 08193-Cerdanyola del Vallès, Catalonia, Spain

<sup>4</sup> Electron Microscopy for Materials Science, EMAT, University of Antwerp, Groenenborgerlaan 171 U430, 2020 Antwerpen, Belgium

## **Abstract**

A methodology of general validity to prepare epitaxial nanocomposite films is reported based on the use of colloidal solutions containing different crystalline preformed oxide nanoparticles (*ex-situ* nanocomposites). The trifluoroacetate (TFA) metal-organic chemical solution deposition route is used with alcoholic solvents to grow epitaxial YBa<sub>2</sub>Cu<sub>3</sub>O<sub>7</sub> (YBCO) films. For that reason stabilizing oxide nanoparticles in polar solvents is a challenging goal. We have used scalable nanoparticle synthetic methodologies such as thermal and microwave-assisted solvothermal techniques to prepare CeO<sub>2</sub> and ZrO<sub>2</sub> nanoparticles. We show that stable and homogeneous colloidal solutions with these nanoparticles can be reached using benzyl alcohol, triethyleneglycol, nonanoic acid, trifluoroacetic acid or decanoic acid as protecting ligands, thereby allowing subsequent mixing with alcoholic TFA solutions. An elaborate YBCO film growth analysis on these nanocomposites allows the identification of the different relevant growth phenomena, e.g. nanoparticle pushing towards the film surface, nanoparticle reactivity, coarsening and nanoparticle accumulation at the substrate interface. Upon mitigation of these effects, YBCO nanocomposite films with high self-field critical currents ( $J_c \sim 3\text{-}4 \text{ MA/cm}^2$  at 77 K) were reached, indicating no current limitation effects associated to epitaxy perturbation, while smoothed magnetic field dependences of the critical currents at high magnetic fields and decreased effective anisotropic pinning behavior confirms the effectiveness of the novel developed approach to enhance vortex pinning. In conclusion, a novel low cost solution-derived route to high current nanocomposite superconducting films and coated conductors has been developed with very promising features.

## **1. Introduction**

In recent years, oxide nanocomposites have been widely developed because an amazing range of new properties or advanced functionalities can be generated through interfaces among dissimilar materials [1-4]. Epitaxial thin films are one of the most popular fields in the nanocomposite landscape because in that case strain engineering allows going even further in

the nanostructure control and so different sorts of self-assembled and randomly distributed nanostructures have been generated with very appealing properties .

Coated conductor (CC) development has been one of the topics where the novel advances in understanding nanocomposite film growth mechanisms have raised a huge interest [5-9]. While achieving epitaxial superconducting structures on top of buffered metallic substrates lead to the first boost in CC performance, a second major boost was obtained via the novel nanocomposite structure generated in  $\text{YBa}_2\text{Cu}_3\text{O}_7$  (YBCO) epitaxial thin films. Here, the challenge was to enhance vortex pinning at high temperatures and high magnetic fields through the generation of artificial pinning centers, i.e. non-superconducting phases or structural defects which can efficiently immobilize the vortices in the presence of Lorentz forces associated to flowing currents. Vacuum (Pulsed Laser Deposition, PLD) or chemical (MOCVD, HLPE) deposition approaches, where YBCO and a secondary phase grow simultaneously, first demonstrated that a huge gain in performance was possible [10-12]. During the last 10 years many efforts have been devoted to optimize the nanostructure and to understand the properties of these materials [13-15].

As a completely different approach, chemical solution deposition (CSD) was introduced to prepare epitaxial YBCO nanocomposite films [14, 16]. The CSD methods excel in their low investment costs and scalability compared to vacuum techniques while the growth mechanisms are deeply modified [17-26]. In this case, complex solutions are prepared where the salts used to prepare YBCO (trifluoroacetates, TFA) are extended to a fourth element (Zr, Hf, Sn, Ta) through soluble metal-organic salts with the desired stoichiometry to achieve secondary phases such as  $\text{BaZrO}_3$ ,  $\text{BaSnO}_3$ ,  $\text{BaHfO}_3$ ,  $\text{Ba}_2\text{YTao}_6$ , etc [16, 27-29]. This single solution precursor leads, after deposition and growth, to a spontaneous segregation of two separate oxide phases (*in-situ* nanocomposite approach). The growth mechanism and final nanostructure was, as expected, completely different from that obtained through vacuum deposition methodologies. In this case, the secondary phases remain randomly distributed within the film while they can remain either randomly oriented or have an epitaxial relationship with the YBCO matrix [30]. These nanocomposites can also display a huge vortex pinning enhancement characterized by outstanding and unique features, such as a strongly reduced superconducting anisotropy [30]. The *in-situ* nanocomposite CSD approach has also been widely investigated in recent years and much progress has been made in controlling the nanostructure and in understanding their physical properties [31-33]. For instance, a thorough analysis of the correlation between nanostrain generated within the YBCO matrix and the pinning force, evidenced that a novel vortex pinning mechanism may become effective in high temperature superconductors (HTS), which is closely associated to local disruption of the superconducting order parameter by tensile strain [30, 34]. On the other hand, the comprehension of the complex growth mechanisms, involving kinetic and thermodynamic effects, forced to use multi-step processing paths to achieve control of the separate nucleation and growth processes of the two crystalline phases forming the nanocomposite [31, 32]. For that reason, it would be worthwhile to define new synthetic routes where an extended compositional spread could be explored and modified nanostructure control paths could be defined. The use of colloidal solutions is now appearing as an alternative potential path for *ex-situ* CSD growth of nanocomposite films. Up to now, however, only limited progress has been made [35, 36].

Here, we present an interdisciplinary investigation of this novel *ex-situ* CSD approach for YBCO epitaxial nanocomposite film growth schematically described in Figure 1, which we anticipate as having a great potential to become a large scale and low cost approach for

manufacturing high magnetic field CCs [37]. The used methodology relies on preparing crystalline oxide nanoparticles through easily scalable, facile solvothermal or microwave-assisted solution methods [38]. The nanoparticles are stabilized in an alcoholic solution, either through the initial use of solvents also behaving as ligands or through ligand exchange [39-43]. The nanoparticle suspension is subsequently mixed and stabilized in the metal-organic TFA precursor solution, used for YBCO film growth, to form a stable colloidal solution with the desired concentration, see Figure 1. A key advantage of this novel approach is that a tight control of the composition, particle size and concentration of the nanoparticles becomes possible. In this work, we report our first study of the complete process associated to this novel growth route, focusing on two different crystalline oxide preformed nanoparticles ( $\text{ZrO}_2$  and  $\text{CeO}_2$ ), and discuss the phenomena we encounter during the nanocomposite growth process. The two selected oxide phases are chemically compatible with YBCO, even if they react to form  $\text{BaZrO}_3$  (BZO) and  $\text{BaCeO}_3$ , respectively, as it is confirmed by the high superconducting transition temperatures achieved. The comprehension of the growth mechanisms taking place has enabled us to achieve high quality epitaxial YBCO nanocomposite films with enhanced vortex pinning capability, as compared to pristine YBCO. Our work stresses the relevance of properly combining the knowledge emanating from the different involved disciplines (solution chemistry, crystal growth, nanostructure characterization, vortex physics) to succeed in generating an adequate working methodology to overcome the many hurdles needing to be confronted. We will finally complete this report with an outlook of the challenges that still exist in the *ex-situ* nanocomposite development and how we expect to tackle them in the future.

## 2. Experimental

The  $\text{ZrO}_2$  and  $\text{CeO}_2$  nanoparticles (NPs) are synthesized using thermal and/or microwave (MW) activation by a solvothermal procedure. In both cases, the temperatures are in the range of  $220^\circ\text{C}$ . In the case of  $\text{ZrO}_2$  an alternative approach using a sealed reactor was also used. For the microwave-assisted treatment a CEM Discover MW at 2.45GHz was used.

**$\text{ZrO}_2$  nanoparticles** are synthesized using thermal or microwave activation, starting from  $\text{ZrCl}_4$  and benzyl alcohol [41, 44, 45]. In the thermal activation route, the precursor is treated at  $220^\circ\text{C}$  for 192 hours in a sealed reactor, leading to elongated monoclinic  $\text{ZrO}_2$  NPs with typical size  $2 \times 8 \text{ nm}^2$ . Only 4 hours treatment at  $220^\circ\text{C}$  is necessary when the microwave activation route is applied, also leading to elongated monoclinic  $\text{ZrO}_2$  NPs with the long edge around 7 nm in size. Both treatments lead to an unstable dispersion directly after synthesis, although a post-modification by a ligand exchange yielded to stable colloidal solutions. For the  $\text{ZrO}_2$  NPs obtained via thermal activation a ligand exchange with decanoic acid, yielded to stable  $\text{ZrO}_2$  colloidal solution in alcoholic media (e.g., methanol, ethanol). The  $\text{ZrO}_2$  NPs obtained via thermal activation were treated with decanoic acid, yielding a stable  $\text{ZrO}_2$  colloidal solution in alcoholic media (e.g., methanol, ethanol). The  $\text{ZrO}_2$  NPs obtained via microwave activation were first treated with dodecanoic acid and oleyl amine, yielding colloidally stable dispersion in chloroform [41, 42]. A subsequent ligand exchange leads to sterically stabilized, via nonanoic acid, or charge stabilized, via trifluoroacetic acid, NPs dispersed in methanol.

**$\text{CeO}_2$  Nanoparticles.** The microwave-assisted solvothermal method was utilized to synthesize  $\text{CeO}_2$  NPs, and by using different precursor solutions, the size of the  $\text{CeO}_2$  NPs were tuned. The precursors solution containing Ce (III) acetylacetonate and triethyleneglycol (TREG) microwave treated at  $220^\circ\text{C}$  for 10 min, yielded small quasi-isomorphous  $\text{CeO}_2$  NPs of 2-3 nm in diameter.

The resulting CeO<sub>2</sub> NPs were precipitated by centrifugation and washed with an ethylacetate-ethanol mixture and finally, redispersed in methanol or ethanol. The initial ligand, TREG, could also be replaced with decanoic acid via a ligand exchange, also leading to stable colloidal solutions in alcohols.

The precursor solution containing Ce (III) acetate and benzyl alcohol [46] produced cubic-like CeO<sub>2</sub> NPs of 5-6 nm in diameter, after a microwave treatment at 220 °C for 10 min. These bigger NPs are stable in benzyl alcohol.

All the described procedure lead to NPs solutions, which are stable in alcoholic media with concentrations of at least 90 mM.

**YBCO anhydrous solution.** The preparation of YBCO solution consists of the dissolution, in an inert atmosphere, of YBCO powder in an excess of trifluoroacetic anhydride (TFAA), a small quantity of TFAH (Aldrich 99%), as catalyst and recently distilled acetone as solvent. The mixture is stirred and heated at 50°C during 72 hours. The resulting solution is filtered and evaporated through vacuum. The mixture of TFA salts (Ba(TFA)<sub>2</sub>, Cu(TFA)<sub>2</sub> and Y(TFA)<sub>3</sub>) is then dissolved in sufficient anhydrous methyl alcohol or dry acetone to give a solution with a total metal ion concentration of 1 - 1.5M [47]. This solution is stored in sealed vials, in an inert atmosphere. The viscosity was measured with a rheometer Haake RheoStress 600 reaching values of 2-5 mPas. The metal stoichiometry is confirmed by titration analysis and the water content has been evaluated by the Karl-Fischer method to be always < 1 wt%.

**YBCO film growth.** YBCO precursor films were deposited on LaAlO<sub>3</sub> (LAO) single crystal substrates (5mm x 5mm) using spin coating with a spinning rate of 6000 rpm for 2 min. The coatings were pyrolyzed in a humid O<sub>2</sub> atmosphere to form nanocrystalline precursor films. The heating rate during the pyrolysis was kept at 3-5 K/min in the temperature range from 100°C to 310°C. Subsequently, the YBCO precursor layers were crystallized at 810 °C in N<sub>2</sub>-0.02% O<sub>2</sub> with 4.2% humidity (dew point 25 °C). In the last stage the crystallized films were annealed at 450 °C for 2 h in a dry oxygen atmosphere.

**Characterization techniques.** The particle size distribution was determined by dynamic light scattering (DLS) which relates the fluctuations in light scattering with the Brownian motion of colloidal particles and calculates a solvodynamic diameter. The particle size distribution of the different samples was determined at 298 K using a Zetasizer Nanoseries instrument Nano-ZS (Malvern Instruments, U.K.). It involves a quasi-elastic light scattering (QELS) analyzer combined with a noninvasive backscatter technology (NIBS). The samples (1.0 mL) were measured directly without dilution. Three subsequent measurements were performed in order to check the reproducibility of the results.

The microstructure and phase analysis of the YBCO nanocomposite films were studied by X-ray diffraction using a Bruker AXS GADDS diffractometer equipped with a 2D detector. Strain quantification was carried out based on the Williamson–Hall method by analyzing the symmetric (00l) 2θ Bragg diffraction integral breadth acquired in a Siemens D5000 diffractometer using Cu Kα. Surface morphology of pyrolyzed and grown films was characterized using optical microscopy (Leica DM 1750 M) and scanning electron microscopy FEI Nova 600 Nanolab Dual-Beam FIB, respectively. Different transmission electron microscopes (TEM) were used for the microstructural analysis. A FEI Tecnai G<sup>2</sup> F20 operated at 200 kV, a FEI Titan 60-300 microscope equipped with a X-FEG gun, a CETCOR probe corrector and a Gatan energy filter TRIDIEM 866 ERS operated in STEM mode at 300 kV.

Transport critical current and resistivity measurements were carried out in a PPMS Quantum Design system provided with a 9 T magnet and variable temperature from 5 to 300 K. Narrow bridges of 200  $\mu\text{m}$  in length and 10 to 30  $\mu\text{m}$  in width were fabricated with standard photolithography with a Durham Magneto Optics Std MicroWriter<sup>TM</sup>. Silver metal contacts were evaporated and post-annealed, ensuring contact resistances below 10  $\mu\Omega$ . Films were measured with the standard four probe method. The applied current was sent parallel to the ab planes and  $J_c$  was determined by using a 10  $\mu\text{Vcm}^{-1}$  criterion. In angular measurements, the magnetic field was rotated from the c axis ( $180^\circ$ ) to the ab plane ( $90^\circ$ ), ensuring the maximum Lorentz force configuration. The angular dependent irreversibility line  $T_{\text{irr}}$  was defined by resistivity measurements using the criterion  $\rho(T_{\text{irr}})/\rho(100\text{K})=10^{-3}$ . The critical temperature of the superconducting patterns corresponds to  $T_c^{\text{onset}}$  and was measured both by resistivity measurements and by inductive measurements with a Superconducting Quantum Interference Device magnetometer (SQUID). This SQUID magnetometer was also used to determine the critical current density using the Bean critical state model of thin discs.

### 3. Results and Discussion

#### 3.1. Preparation of colloidal YBCO solutions

Growth by CSD of YBCO nanocomposites from preformed nanoparticles (*ex-situ* nanocomposites) is a challenging process, see a general layout in Figure 1. We needed to identify synthetic methods to prepare metal oxide nanoparticles of small sizes (2-10 nm) and narrow size distribution ( $\pm 1-2$  nm) at large concentrations (25 - 375 mM) and in polar dispersants. Metal oxide nanoparticles are scarcely stable in alcoholic media at high concentrations, thus new knowledge had to be generated in this direction. In addition, the presence of yttrium, barium and copper carboxylate salts in the final YBCO precursor solutions infer a highly ionic environment hampering an easy stabilization of the nanoparticles. Adequate stabilizing agents needed to be identified for each specific case.

The stable YBCO precursor colloidal solution with the preformed nanoparticles needs then to be deposited on a substrate and therefore a fine control of the rheology of the solution is mandatory to obtain a homogeneous deposited film. This homogeneity needs to be ensured also after the pyrolysis of the metalorganic precursors, otherwise further tuning of the solution formulation will be required.

In the next sections we present some successful cases of our effort of synthesizing metal oxide nanoparticles, stabilization methods and routes encountered to reach homogeneous pyrolysis.

##### 3.1.1. Nanoparticle synthesis

Various synthetic methods are available to prepare nanoparticles [48-53]. However, we focus on thermal and microwave-assisted solvothermal synthesis, using environmentally friendly solvents, e.g. benzyl alcohol, triethylenglycol, isopropanol, ethanol and water [39-43, 54]. This is an interesting technique for large scale production compared to the previously published microemulsion approach [35], which shows a more limited capability to adapt to different NP compositions.

Elongated, monoclinic  $\text{ZrO}_2$  NPs (long edge 7 – 15 nm) are obtained using either a thermal or MW activation via a solvothermal procedure (Figures 2a, 2b and 3a). So, similar results are obtained for both methods, although using the microwave method leads to a reaction time

reduction by a factor of 48. The  $ZrO_2$  NPs, via thermal activation, form stable suspensions in methanol by the aid of decanoic acid, showing a solvodynamic diameter of 12-14 nm according to DLS (Figure 4a). While the  $ZrO_2$  NPs, via microwave activation, can be sterically stabilized similar to the thermal activated NPs, using nonanoic acid, or charge stabilized, using TFA, in methanol. This is confirmed by DLS analysis, yielding a solvodynamic diameter of 11 – 12 nm for the steric and charge stabilized NPs in methanol (Figure 4a).

Quasi-isomorphous, cubic  $CeO_2$  NPs are obtained using microwave assisted synthesis (Figures 2c, 2d, 2e and 3b). The NP's size can be varied depending on the used precursor.  $Ce(acac)_3$  in TREG yields NPs of 2 – 3 nm in diameter, leading to a solvodynamic diameter of 5-8 nm according to DLS (Figure 4c). Here, TREG also acts as stabilizing molecule, which can be exchanged by decanoic acid, leading to a solvodynamic diameter of 10 nm.  $Ce(Ac)_3$  in benzyl alcohol, on the other hand, leads to NPs of 5 – 6 nm in diameter (Figure 4c) and a solvodynamic diameter of 5 nm.

### 3.1.2. Nanoparticles stabilization in YBCO precursor solutions

Stabilization in TFA-YBCO precursor solutions is not straightforward, since the precursor exhibits an alcoholic and highly ionic environment due to the Y, Ba, Cu metal-salts. Sometimes, adequate stabilization requires of a post treatment.

The  $ZrO_2$  elongated NPs, sterically stabilized with decanoic acid in methanol, obtained via thermal activation, can be introduced in the methanol-based TFA-YBCO precursor solution up to 24 mol %. DLS measurements (Figure 4b) confirm the presence of individual NPs in suspension, with a solvodynamic diameter of about 13 nm. However, the suspensions are only stable for less than two days. Uniform aggregates are formed after two days, with a solvodynamic diameter of around 100 nm.

The  $ZrO_2$  NPs, obtained via microwave activation, can be transferred to the methanol-based YBCO precursor solution, through steric (via nonanoic acid) or charge (via TFA) stabilization. As these NPs are first stabilized in apolar solvents (e.g., chloroform) via dodecanoic acid and oleyl amine, the stability after ligand exchange (with nonanoic acid or TFA) is first assessed in pure methanol, via DLS measurements (Figure 4a). The  $ZrO_2$  NPs give rise to a solvodynamic diameter of about 12 nm, independently on the stabilization procedure, indicating that the NPs are individual in pure methanol. The introduction of the NPs in the YBCO precursor renders a similar solvodynamic diameter, showing the successful addition of the NPs to the YBCO solution. These  $ZrO_2$  NPs, steric or charge stabilized, can be stabilized up to a concentration of 50 mol % and remain stable for at least 2 months without any sign of agglomeration.

The small  $CeO_2$  NPs (2-3 nm in diameter), stabilized in TREG, can be transferred to the TFA-YBCO precursor solution up to 32 mol %. DLS analysis shows a solvodynamic diameter of about 8-10 nm for a period of time of at least 1 month (Figure 4c). However, due to the presence of large amounts of TREG, inhomogeneous pyrolysis are obtained (Figure 5a) and a ligand exchange with decanoic acid was attained producing TFA-YBCO suspensions up to 16 mol % of NPs. These new suspensions, stable for 3-4 days, successfully produced homogeneous pyrolyzed layers (see Figure 5b). The larger  $CeO_2$  NPs (5-6 nm in diameter) with benzyl alcohol are also successfully introduced in the TFA-YBCO precursor solution, again up to 32 mol %. DLS measurements gave solvodynamic diameters of 10-12 nm and the solutions were stable for longer period of time (7 days), see Figure 4c. These solutions lead to homogeneous pyrolysis, see Figure 5b.

### 3.2. Growth and characterization of nanocomposites

Depending on the nanoparticles composition, size and surface chemistry, different situations are encountered after the growth process. Next we revise several of the growth phenomena that might dominate the microstructure of the *ex-situ* nanocomposites and that need to be tackled properly.

#### 3.2.1. Pushing of the nanoparticles to the YBCO film surface: CeO<sub>2</sub> nanoparticles

The pushing/trapping phenomena of an insoluble particle at an advancing solid-liquid interface during solidification have been well described in various materials [55-58]. The interaction of the particle with the solid-liquid interface produces forces (drag force and force due to interfacial energy,  $\Delta\sigma_0$ ) resulting in either pushing of the particle along the solidification front or trapping of the particle in the solid. The interaction of particles at the interface is influenced by various parameters such as the size of the particle,  $r^*$ , and the critical growth rate,  $R^*$ , see equation 1.

$$R^* \propto \frac{\Delta\sigma_0}{\eta r^*} \quad \text{eq.1}$$

where  $\eta$  is a viscosity term. Accordingly, small nanoparticles appear to be pushed out of the growth interface whereas larger nanoparticles tend to be trapped [59]. We have also identified this process for the CeO<sub>2</sub> nanoparticles in the present TFA route even if the growth mechanism strongly differs from the melt processing approach [14, 58, 60].

Spin-coated CeO<sub>2</sub> NPs-YBCO nanocomposite thin films on LAO single crystals have been investigated using two different NP sizes, 2 nm and 6 nm  $\pm$  2nm.

The 2 nm CeO<sub>2</sub> NPs-YBCO films lead to highly epitaxial *c*-axis oriented YBCO films for the whole range of CeO<sub>2</sub> concentrations (0-10 mol %) here studied. Typical 2D XRD  $\theta$ -2 $\theta$  scan obtained for CeO<sub>2</sub>-YBCO nanocomposites is shown in Figure 6a. From the integrated spectra, Figure 6b, the presence of BaCeO<sub>3</sub> is also identified, thus, confirming that reactivity between BaF<sub>2</sub> with CeO<sub>2</sub> occurs during the growth process [61]. The crystallite size calculated from the Scherrer formula results in 25 nm. The formation of dense YBCO nanocomposites with homogeneous surface morphology is confirmed by SEM analysis, see Figure 6c. By TEM analysis it is confirmed the formation of highly epitaxial YBCO films but also the inhomogeneous distribution of the CeO<sub>2</sub> NPs. The majority of the CeO<sub>2</sub> NPs preserve their original size but they are segregated at the YBCO film surface, see Figure 7a. Also, some reactivity with BaF<sub>2</sub> forming BaCeO<sub>3</sub> is identified, as previously anticipated by XRD. The accumulation of nanoparticles at the film surface therefore results from the pushing behavior of foreign particles described above [55, 57].

The nanostrain ( $\varepsilon$ ) generated in the YBCO matrix as a consequence of the incorporation of the nanoparticles [30], can be quantified by means of an accurate analysis of x-ray diffraction peak broadening. The Williamson–Hall method has been proved successful to determine non-homogeneous strain and differentiate it from the coherent volume size. The nanostrain displayed in YBCO–CeO<sub>2</sub> nanocomposites is higher than in pristine YBCO films:  $\varepsilon$  increases from 0.09% (pristine YBCO) to 0.18% (8% mol CeO<sub>2</sub>).

Larger CeO<sub>2</sub> nanoparticles (~ 6 nm, see figure 4) can be trapped within the YBCO matrix (Figures 7b and 7c) indicating that the critical radius  $r^*$  to trap particles (eq. 1) has been reached

at the present growth rate [62]. Of course, an equivalent approach to trap small nanoparticles is, as suggested by eq. (1), to increase the YBCO film growth rate  $R^*$  through processing parameters such as  $P_{H_2O}$  or  $P_T$  [63, 64]. From the microstructural analysis of these films, Figures 7b and 7c, we observe the formation of highly epitaxial YBCO films, although reactivity was not avoided, resulting in  $BaCeO_3$  NPs around 20 nm in size. Interestingly, from TEM analysis, it is observed that most of the  $BaCeO_3$  NPs are trapped in the YBCO matrix, thus demonstrating the limitation to pushing effect by modifying, in this case, the initial NP size, Figure 7b. According to STEM analysis, we observe that some nanoparticles are randomly oriented and some are epitaxially grown at the LAO substrate interface (Figure 7c), suggesting that the reactivity has occurred after the YBCO growth [61]. In this case, the generated nanostrain is increased up to 0.15 %, as compared to 0.09 % in pristine YBCO, probably due to an enhanced concentration of stacking faults (see Figures 7(a) and 7(b)), as usually observed in YBCO in-situ grown nanocomposites.

The analysis of the superconducting properties of the 8 mol %  $CeO_2$ -nanocomposite with 2-nm preformed nanoparticles, exhibit a  $T_c$  of 90 K and a self-field critical current density at 77 K of 2 MA/cm<sup>2</sup>, compared to  $T_c = 91$  K and  $J_c = 4$  MA/cm<sup>2</sup> at 77K for a pristine TFA YBCO film, obtained from 4-point transport measurements (Figure 8a). Notice that the nanocomposite's  $J_c$  lies slightly below that of the standard film over the complete magnetic field range. However, the normalized  $J_c(H)$  dependence of both samples (to its corresponding  $J_c$  at self-field,  $J_c^{sf}$ ), (see Figure inset of Figure 8a) shows that at intermediate fields, between 0.02 T and 2 T, the nanocomposite dependence lies above that of the standard film. Notice also that  $H^*$  as a function of the temperature, defined as the magnetic field where the plateau of  $J_c$  in a log-log plot deviates to a power law, is also larger for the nanocomposite film (Figure 8b).  $H^*$  is assigned to the crossover field between a single vortex pinning and a collective pinning regime, and therefore it is an indication of the density and effectiveness of individual pinning centres. Therefore, results shown from the  $CeO_2$ -nanocomposite suggest that some modifications of the YBCO microstructure have occurred in the direction of improving field dependences. At magnetic fields higher than 2T, we encounter a stronger decrease of the  $J_c(H, 77K)$  dependence for the nanocomposite, which suggest that its irreversibility field lies below that of the pristine film. This is confirmed in Figure 9a, indicating the irreversibility lines of three of the films analyzed in this paper normalized to their respective  $T_c$ . If we concentrate, for the moment, on the data of the  $CeO_2$ -nanocomposite and we compare them with the best pristine film, a decrease of the irreversibility line is indeed confirmed at similar levels of previously reported pristine films [65]. The decrease of the irreversibility line can be partially ascribed to the decrease of twin boundary pinning in nanocomposites due to their shorter vertical coherence, as recently reported [66, 67].

Finally, Figure 9b shows the effective irreversibility field as function of the irreversibility temperature for the  $CeO_2$  NPs sample measured at different angles  $\theta$  between the magnetic field and the sample surface. Remind you that the effective irreversibility field is given by equation 2 following a Blatter-scaling approach [68],

$$H_{eff} = H\sqrt{\cos^2(\theta) + \gamma^{-2}\sin^2(\theta)} \quad \text{Eq 2.}$$

and that between an angular range of 70° and 40°, where only the isotropic defects contribution is present,  $H_{irr}^{eff}$  ( $T_{irr}$ ) should collapse with a effective anisotropy,  $\gamma_{eff}$ , as previously reported [69]. This analysis allows us to identify the effective anisotropy,  $\gamma_{eff}$ , associated to this nanocomposite and compare it with that of the standard YBCO film and in-situ CSD

nanocomposites. Notice that whereas  $\gamma_{\text{eff}}=5-7$  for YBCO [70], this is reduced down to 2.4 for the CeO<sub>2</sub>-nanocomposite. This is in agreement with that observed in CSD *in-situ* nanocomposites [13, 30]. Therefore, we can anticipate that the effective anisotropy of *ex-situ* nanocomposites behaves similar to that of *in-situ* ones, and it is much reduced as compared to pristine YBCO film, which makes these nanocomposites highly interesting for applications.

Analysis of the superconducting properties of CeO<sub>2</sub>-nanocomposites with larger pre-formed nanoparticles, although minimized the pushing effects, showed  $J_c^{\text{sf}}(77\text{K}) = 0.5 \text{ MA/cm}^2$ . Thus, demonstrating that the overall  $J_c^{\text{sf}}$  is lower than that of the smaller CeO<sub>2</sub>-nanoparticles and therefore that in this case, effort should be devoted to minimize nanoparticles coarsening and avoid possible current blocking effects [71].

So, by modifying the preformed CeO<sub>2</sub> NP size, we are able to obtain epitaxial YBCO nanocomposites with increased nanostrain. The reactivity between the BaF<sub>2</sub> intermediate phase and CeO<sub>2</sub> NPs does not compromise the YBCO nanocomposite performance although further optimization would be required to further improve the pinning properties.

### 3.2.2. Accumulation of nanoparticles at the substrate interface: ZrO<sub>2</sub> nanoparticles

Another phenomenon that may occur when growing *ex-situ* nanocomposites, is the accumulation of NPs at the substrate interface.

A series of ZrO<sub>2</sub>-YBCO nanocomposites (0 – 10 mol %) were prepared, using the charge stabilized ZrO<sub>2</sub> NPs, obtained via MW activation, The resulting YBCO films are epitaxial according to the (00l) reflections in the  $\theta-2\theta$  XRD patterns, although the 10 mol % ZrO<sub>2</sub>-YBCO film also gives rise to randomly oriented YBCO, as seen by the (103) reflection (Figure 10a). This suggests that high NP loadings lead to random and thus poorly grown YBCO [31], which is also confirmed by the 2D-XRD patterns in Figure 10c. Furthermore, the 10 mol % ZrO<sub>2</sub> NPs-YBCO nanocomposite film shows the presence of BZO in the final layer, while ZrO<sub>2</sub> reflections remain absent (Figures 10a and 10b). Hence, the initial ZrO<sub>2</sub> NPs are transformed to BZO NPs, similar to the transformation of CeO<sub>2</sub> to BaCeO<sub>3</sub> (section 3.2.1) [31].

The magnetic field dependence of the critical current density normalized over self-field,  $J_c/J_c^{\text{self}}(\text{H})$ , of the 0, 1, and 3 mol-% ZrO<sub>2</sub> NPs – YBCO films has been analyzed by SQUID and represented in Figure 11. It can be concluded from this graph that the  $J_c/J_c^{\text{self}}(\text{H})$  dependency is better for the 3 mol % ZrO<sub>2</sub> NC addition at higher magnetic fields, although the critical current density at 77 K in self-field decreases. As previously been stated in literature, epitaxial YBCO growth can be promoted via the introduction of a thin YBCO seed layer [30, 71]. Hence, a thin, pure YBCO precursor seed layer was pyrolyzed in between the LAO substrate and a nanocomposite film containing 10 mol % of preformed ZrO<sub>2</sub> NPs, which was subsequently grown. Now, the film only shows (00l) YBCO reflections, indicating c-axis YBCO orientation, according to the XRD diffraction patterns in Figures 10a and 10b, which demonstrates that the seed layer has a good effect on the nanocomposite film growth.

From TEM analysis it becomes clear in Figures 12a, that already the 3 mol % nanocomposite without seed layer shows the presence of some Zr-atoms at the substrate interface. Instead, if the pure YBCO seed layer was deposited between the substrate and the nanocomposite, the formed BZO NPs are distributed in the top YBCO layer keeping a fairly good homogeneous distribution. So, the use of an YBCO seed layer clearly hinders the diffusion of the NPs to the LAO substrate. Also, the NPs present in the layer are grown from the initial 7 nm ZrO<sub>2</sub> NPs to

12 – 25 nm of BZO NPs (Figure 12b), which can be due to transformation of  $ZrO_2$  to BZO. It's also significant to note that BZO NP pushing to the film surface is minimized in this case (Figure 12b).

So, also microstructural analysis confirms that by using a seed layer, YBCO grows epitaxial, suggesting that otherwise YBCO and BZO nucleation compete at the substrate interface. This tendency might be tunable to some degree, in any case, through selection of the heating profile to minimize long range atomic diffusion.

In this case, the superconducting properties have been analyzed by SQUID. There is no change on  $T_c$  ( $T_c = 90$  K) and  $J_c^{sf}(77K) = 4$  MA/cm<sup>2</sup>, i.e. they are again at the best values of our standard films concerning self-field critical currents while preliminary analysis of vortex pinning properties show promising performance.

### 3.2.3 Reactivity and coarsening of the nanoparticles in the YBCO film

When single metal oxides, like  $ZrO_2$  or  $CeO_2$  nanoparticles are chosen, a large tendency exists to react with the Ba, giving rise to perovskite structure  $BaMO_3$  ( $M = Zr, Ce$ ) [6, 61, 72, 73]. An undesirable consequence of this reaction is that cation stoichiometry becomes slightly uncompensated and so some  $Y_2Cu_2O_5$  NPs remain which can be either pushed to the surface or trapped in the YBCO matrix and thus may play some role as current limiting defects (Figure 12b). In this section we will focus on the reaction and coarsening process of the  $ZrO_2$  elongated NPs obtained via thermal activation route described above (section 3.1.1), even though the main trends should also be valid for  $CeO_2$  NPs.

A series of YBCO- $ZrO_2$  nanocomposites have been prepared by spin-coating on LAO varying the concentration up to 24 mol %. From XRD analysis, highly epitaxial c-axis oriented YBCO is obtained for all concentrations. Also, the formation of epitaxial BZO NPs is identified, see figure 13a and 13b. HR-STEM analysis identifies two different scenarios (1) coarsening of randomly oriented BZO NPs and, eventually, coalescence (Figure 14a) and (2) epitaxial BZO NPs nucleated on the substrate surface, Figure 14b. The occurrence of both phenomena is a characteristic of CSD nanocomposites, as also reported in *in-situ* nanocomposites [30]. From the Z-contrast image, Figure 14c, the formation of a high density of stacking faults (horizontal dark stripes) is also identified here. It is well known that the incorporation of randomly oriented nanoparticles in the YBCO matrix strongly enhance the formation of these microstructural defects as a mechanism to reduce the strain accumulated at the incoherent interfaces of the nanoparticles with the YBCO matrix, and thus, generating nanostrain [30, 31]. Indeed, the nanostrain is continuously increased with  $ZrO_2$  concentration, from 0.11 % (pristine) to 0.26 % (24% mol  $ZrO_2$ ), see Figure 13c.

Thus, for the YBCO- $ZrO_2$  nanocomposite system here described, it is confirmed that reactivity exists inducing strong coarsening effects, similar to the nanocomposites described in sections 3.2.1 and 3.2.2. Therefore, tight control of the kinetics during the growth process will be required for fine tuning of the coarsening rate [31] and the defect structure associated to randomly oriented nanoparticles with a subsequent improvement of the pinning properties.

The analysis of the superconducting properties of the YBCO-16 mol %  $ZrO_2$  nanocomposites enables us to conclude that  $T_c = 90$  K and  $J_c^{sf}(77 K) = 4$  MA/cm<sup>2</sup>, thus reaching  $J_c^{sf}$  values of our best pristine samples, see Figure 15a [30, 31]. The  $J_c(H)$  dependence is rather rounded-like, as typically observed for *in-situ* CSD nanocomposites. In addition, between 0.1 T and 2 T, we

demonstrate that the actual  $J_c$  at 77 K from the nanocomposites is always larger than that of the standard film. Only for magnetic fields above 2T, we encounter a decrease of  $J_c$  below that of the standard film that we ascribe to a decrease of the irreversibility line (see Figure 9a). In this case, the decrease is much smaller than for the CeO<sub>2</sub>-nanocomposite, and it is inexistent for H//ab. Overall, it suggests that twin boundary pinning when H//c is diminished in these nanocomposites. This can be further confirmed in Figure 15b, where we represent the  $J_c(\theta)$  dependence for the BZO-nanocomposite and the standard film at high magnetic fields, now at 65K. Notice that the twin boundary peak usually observed at H//c disappears for the nanocomposite, thus evidencing that the twin boundary c-axis correlation is broken by a high density of stacking faults, as previously reported in CSD *in-situ* nanocomposites [66, 74]. In addition, the peak for H//ab is much broader for the ZrO<sub>2</sub> nanocomposites than the pristine film, confirming that the density of stacking faults and their effectiveness as vortex pinning centres is very relevant in these *ex-situ* nanocomposites. These results are in clear agreement with the microstructural analysis of this sample (Figure 11c), which demonstrated a high density of stacking faults.

Finally, further analysis of the angular dependence of the irreversibility line, Figure 15c, demonstrate here too that the effective anisotropy,  $\gamma_{\text{eff}}=3$ , is heavily reduced. Hence, we can conclude that these *ex-situ* BZO nanocomposites, though should be further optimized, are presenting very tempting properties which corroborate those vortex pinning characteristics of previously studied *in-situ* nanocomposites.

We can therefore conclude that ZrO<sub>2</sub> nanoparticles prepared via MW or thermal activation are very promising, though their reactivity, coarsening and segregation effects should be further investigated to minimize them. If that goal is successfully achieved, we envisage very promising *ex-situ* BZO nanocomposites.

#### 4. Conclusions and outlook

In summary, this work has evidenced for the first time that the colloidal solution approach can indeed lead to high quality epitaxial nanocomposite films and so we envisage that this *ex-situ* methodology will have a strong impact in the near future in the development of low cost high current CCs.

We have particularly focused on several different situations that might rise when growing nanocomposite films from chemical solutions including preformed nanoparticles. We want to emphasize, however, that the examples presented here should be taken only as typical cases which should at this stage not be directly linked to a particular ligand or nanoparticle synthesis method. Upon all the knowledge generated here, several strategies should be considered to overcome the difficulties encountered in any of these or other cases, which suggests that much room for performance improvement exists.

Owing to the complex preparation and processing methodologies here devised for the *ex-situ* growth approach it's worth to conclude with a summary of the route followed which mentions most of the encountered hurdles, already mentioned in the previous sections, thus helping to provide an outlook into the future of this approach. Figure 16 schematizes the different steps involved in the *ex-situ* approach which we now discuss in some detail.

The first step is the synthesis of oxide nanoparticles, with the right composition and size, through a thermal/microwave assisted solvothermal solution approach leading to stable

suspensions in alcohols. Here the main hurdles are to reach a narrow size distribution, to keep the nanoparticles non-agglomerated and to keep the solution stable in a significant long term. The use of facile solvothermal or microwave-assisted heating treatments has been found to be particularly attractive for those purposes showing the potential of these easily scalable synthetic procedures. It was also particularly challenging to find adequate ligands allowing dispersing the nanoparticles in the organic polar solvents used to grow YBCO films, such as TFA precursors. Finally, an additional great advantage of our procedure is that it has a very general validity and so it should be applicable for many more systems.

The second step is related to the preparation of a porous solid precursor film of the right thickness through solution deposition, drying and pyrolysis of the metalorganic precursors. The main goal here was in the case of the ex-situ approach to keep the macroscopic and microscopic homogeneity usually achieved in the standard CSD YBCO process. Several methodologies can be used for deposition (spin or dip coating, web coating, ink jet printing) which require solutions with modified rheological properties and so the actual successful conditions to reach this goal may differ. Some specific ligands used to stabilize the nanoparticles were found to degrade the thickness homogeneity while in other cases it was found that some nanoparticle precipitation could occur at the substrate interface. These are certainly issues that will require a thorough scrutiny in any selection of the stabilizing ligands for specific colloidal solutions. Therefore, it's clear that the choice of the solvents and stabilizing agents, the initial size of the nanoparticles, the deposition method and the thermal treatments are closely related issues that have a strong influence on the final observed phenomena. Once a fairly good homogeneity is obtained in the nanoporous precursor films the usual nucleation and growth process needs to be carried out at high temperature. These steps may become critical if there's a tendency of the nanoparticles to react with the YBCO metal-organic precursors, as it's the case here. When the  $ZrO_2$  or  $CeO_2$  nanoparticles react with Ba to form  $BaZrO_3$  and  $BaCeO_3$ , respectively, it becomes possible to induce some particle coarsening, and eventually coalescence and aggregation, or also that some excessive heterogeneous nucleation occurs at the substrate interface which then would perturb the correct epitaxial growth of the YBCO film. Concerning the coarsening effect it's very likely that it's closely linked to the reactivity of the nanoparticles because a full structural reconstruction occurs. This effect should be probably reduced to a certain extent in non-reactive nanoparticles, although this need to be further investigated. Additionally, the degree of nanoparticle coarsening should be in principle tunable to some extent through accurate selection of the growth temperature and the film growth rate. The second perturbing effect, i.e. interfacial nucleation, is probably not a general trend and, in any case as we have shown here, it can be finely tuned through selection of the substrate cap layer to promote an enhanced YBCO nucleation over BZO or through selection of other parameters controlling the nucleation rate. An additional issue that needs to be taken into account during the film growth step is the nanoparticle pushing effect, i.e. generating an inhomogeneous final distribution of the nanoparticles across the nanocomposite film due to the influence of the interfacial energy between YBCO and the corresponding nanoparticles which generates a dragging force towards the surface. The dragging force associated to this effect is specific to each nanoparticle through the corresponding interfacial energy and so it can have different strengths in different nanoparticles. In any case, it can be tuned through selection of the nanoparticle size and growth rate of the film. The effect, therefore, can be handled, as we have actually shown here in the case of  $CeO_2$  NPs.

Controlling the nanostructure and vortex pinning properties in ex-situ nanocomposites will be a tantalizing issue and much more investigation is required to achieve a full understanding of the correlation between synthesis and processing methodologies with the final defect structure and the concomitant vortex pinning efficiency. The present work has shown that the objective of achieving macroscopic homogeneity of nanoparticle distribution and epitaxy quality and so avoiding superconducting granularity effects can be achieved. On the other hand, although our work suggests that the nanostructure of *ex-situ* nanocomposites will be closely correlated with the mechanisms described for *in-situ* CSD YBCO nanocomposites, it is too early to reach meaningful conclusions concerning the relative merit of both approaches and further investigation is required.

In conclusion, we have shown for the first time that the *ex-situ* nanocomposite approach to epitaxial YBCO nanocomposites can be used as a practical methodology based on easily scalable methodologies and we have also demonstrated that vortex pinning enhancement can be indeed achieved with this novel and wide spectrum approach. We have selected very robust NP synthesis approaches leading to homogeneous size NPs fulfilling the requirements for enhancing vortex pinning. We have also identified the most challenging hurdles needed to be tackled in each of the different steps of this overall complex materials growth process. We do hope that through a deeper understanding of the mutual influence of the different relevant chemical, microstructural and physical effects involved in this methodology we will be able to prepare nanocomposite thin films and CCs with the highest performance using colloidal solutions and *ex-situ* growth approach.

## Acknowledgements

All authors acknowledge the EU (EU-FP7 NMP-LA-2012-280432 EUROTAPES project). ICMAB acknowledges MINECO (MAT2014-51778-C2-1-R) and Generalitat de Catalunya (2014SGR 753 and Xarmae). UGhent acknowledges the Special Research Fund (BOF), the Research Foundation Flanders (FWO) and the Institute for the Promotion of Innovation through Science and Technology in Flanders (IWT). TEM microscopy work was conducted in the Catalan Institute of Nanoscience and Nanotechnology (ICN2). Authors acknowledge the ICN2 Electron Microscopy Division for offering access to their instruments and expertise. Part of the STEM microscopy work was conducted in “Laboratorio de Microscopias Avanzadas” at the Instituto de Nanociencia de Aragon-Universidad de Zaragoza. Authors acknowledge the LMA-INA for offering access to their instruments and expertise. J.G. and M.C. also acknowledge the Ramon y Cajal program (RYC-2012-11709 and RYC-2013-12448 respectively).

## References

- [1] MacManus-Driscoll J L, Zerrer P, Wang H Y, Yang H, Yoon J, Fouchet A, Yu R, Blamire M G and Jia Q X 2008 Strain control and spontaneous phase ordering in vertical nanocomposite heteroepitaxial thin films *Nat. Mater.* **7** 314
- [2] MacManus-Driscoll J L 2010 Self-Assembled Heteroepitaxial Oxide Nanocomposite Thin Film Structures: Designing Interface-Induced Functionality in Electronic Materials *Adv. Funct. Mater.* **20** 2035
- [3] Moshnyaga V, Damaschke B, Shapoval O, Belenchuk A, Faupel J, Lebedev O I, Verbeeck J, Van Tendeloo G, Mucksch M, Tsurkan V, Tidecks R and Samwer K 2003

- Structural phase transition at the percolation threshold in epitaxial  $(\text{La}_{0.7}\text{Ca}_{0.3}\text{MnO}_3)_{(1-x)}:(\text{MgO})_x$  nanocomposite films *Nat. Mater.* **2** 247
- [4] Zheng H, Wang J, Lofland S E, Ma Z, Mohaddes-Ardabili L, Zhao T, Salamanca-Riba L, Shinde S R, Ogale S B, Bai F, Viehland D, Jia Y, Schlom D G, Wuttig M, Roytburd A and Ramesh R 2004 Multiferroic  $\text{BaTiO}_3\text{-CoFe}_2\text{O}_4$  nanostructures *Science* **303** 661
- [5] Malozemoff A P, Fleshler S, Rupich M, Thieme C, Li X, Zhang W, Otto A, Maguire J, Folts D, Yuan J, Kraemer H P, Schmidt W, Wohlfart M and Neumueller H W 2008 Progress in high temperature superconductor coated conductors and their applications *Supercond. Sci. Technol.* **21** 034005
- [6] Selvamanickam V, Chen Y, Shi T, Liu Y, Khatri N D, Liu J, Yao Y, Xiong X, Lei C, Soloveichik S, Galstyan E and Majkic G 2013 Enhanced critical currents in  $(\text{Gd,Y})\text{Ba}_2\text{Cu}_3\text{O}_x$  superconducting tapes with high levels of Zr addition *Supercond. Sci. Technol.* **26** 035006
- [7] Obradors X and Puig T 2014 Coated conductors for power applications: materials challenges *Supercond. Sci. Technol.* **27** 044003
- [8] Yuh S, Takahiro T and Masateru Y 2012 Overview of Materials and Power Applications of Coated Conductors Project *Jpn. J. Appl. Phys.* **51** 010007
- [9] Larbalestier D, Gurevich A, Feldmann D M and Polyanskii A 2001 High-Tc superconducting materials for electric power applications *Nature* **414** 368
- [10] MacManus-Driscoll J L, Foltyn S R, Jia Q X, Wang H, Serquis A, Civale L, Maiorov B, Hawley M E, Maley M P and Peterson D E 2004 Strongly enhanced current densities in superconducting coated conductors of  $\text{YBa}_2\text{Cu}_3\text{O}_{7-x}+\text{BaZrO}_3$  *Nat. Mater.* **3** 439
- [11] Kang S, Goyal A, Li J, Gapud A A, Martin P M, Heatherly L, Thompson J R, Christen D K, List F A, Paranthaman M and Lee D F 2006 High-performance high-Tc superconducting wires *Science* **311** 1911
- [12] Xu A, Delgado L, Khatri N, Liu Y, Selvamanickam V, Abraimov D, Jaroszynski J, Kametani F and Larbalestier D C 2014 Strongly enhanced vortex pinning from 4 to 77 K in magnetic fields up to 31 T in 15 mol.% Zr-added (Gd, Y)-Ba-Cu-O superconducting tapes *APL Mat.* **2** 046111
- [13] Obradors X, Puig T, Palau A, Pomar A, Sandiumenge F, Mele P and Matsumoto K 2010 *Comprehensive Nanoscience and Technology* Andrews D, Scholes G, Wiederrecht G (Amsterdam:Elsevier) 303
- [14] Obradors X, Puig T, Ricart S, Coll M, Gazquez J, Palau A and Granados X 2012 Growth, nanostructure and vortex pinning in superconducting  $\text{YBa}_2\text{Cu}_3\text{O}_7$  thin films based on trifluoroacetate solutions *Supercond. Sci. Technol.* **25** 123001
- [15] Matsumoto K and Mele P 2010 Artificial pinning center technology to enhance vortex pinning in YBCO coated conductors *Supercond. Sci. Technol.* **23** 014001
- [16] Gutierrez J, Llordes A, Gazquez J, Gibert M, Roma N, Ricart S, Pomar A, Sandiumenge F, Mestres N, Puig T and Obradors X 2007 Strong isotropic flux pinning in solution-derived  $\text{YBa}_2\text{Cu}_3\text{O}_{7-x}$  nanocomposite superconductor films *Nat. Mater.* **6** 367
- [17] Lange F F 1996 Chemical Solution Routes to Single-Crystal Thin Films *Science* **273** 903
- [18] Obradors X, Puig T, Pomar A, Sandiumenge F, Mestres N, Coll M, Cavallaro A, Romà N, Gázquez J, González J C, Castaño O, Gutierrez J, Palau A, Zalamova K, Morlens S, Hassini A, Gibert M, Ricart S, Moretó J M, Piñol S, Isfort D and Bock J 2006 Progress towards all-chemical superconducting  $\text{YBa}_2\text{Cu}_3\text{O}_7$ -coated conductors *Supercond. Sci. Technol.* **19** S13
- [19] Martin W R, Xiaoping L, Cees T, Srivatsan S, Steven F, David T, Elliot T, Jeff S, Joseph L, David B, Ken D, James I, Paul C and James S 2010 Advances in second generation high temperature superconducting wire manufacturing and R&D at American Superconductor Corporation *Supercond. Sci. Technol.* **23** 014015
- [20] Vilardell M, Granados X, Ricart S, Van Driessche I, Palau A, Puig T and Obradors X 2013 Flexible manufacturing of functional ceramic coatings by inkjet printing *Thin Solid Films* **548** 489

- [21] Obradors X, Puig T, Gibert M, Queralto A, Zabaleta J and Mestres N 2014 Chemical solution route to self-assembled epitaxial oxide nanostructures *Chem. Soc. Rev.* **43** 2200
- [22] Pollefeyt G, Clerick S, Vermeir P, Feys J, Hühne R, Lommens P and Driessche I V 2014 Ink-jet printing of SrTiO<sub>3</sub> buffer layers from aqueous solutions *Supercond. Sci. Technol.* **27** 095007
- [23] Feys J, Vermeir P, Lommens P, Hopkins S C, Granados X, Glowacki B A, Baecker M, Reich E, Ricard S, Holzapfel B, Van Der Voort P and Van Driessche I 2012 Ink-jet printing of YBa<sub>2</sub>Cu<sub>3</sub>O<sub>7</sub> superconducting coatings and patterns from aqueous solutions *J. Mater. Chem.* **22** 3717
- [24] Driessche I V, Feys J, Hopkins S C, Lommens P, Granados X, Glowacki B A, Ricart S, Holzapfel B, Vilardell M, Kirchner A and Bäcker M 2012 Chemical solution deposition using ink-jet printing for YBCO coated conductors *Supercond. Sci. Technol.* **25** 065017
- [25] Coll M, Pomar A, Puig T and Obradors X 2008 Atomically Flat Surface: The Key Issue for Solution-Derived Epitaxial Multilayers *Appl. Phys. Express* **1** 121701
- [26] Obradors X, Martínez-Julián F, Zalamova K, Vlad V R, Pomar A, Palau A, Llordés A, Chen H, Coll M, Ricart S, Mestres N, Granados X, Puig T and Rikel M 2012 Nucleation and mesostrain influence on percolating critical currents of solution derived YBa<sub>2</sub>Cu<sub>3</sub>O<sub>7</sub> superconducting thin films *Physica C* **482** 58
- [27] Coll M, Ye S, Rouco V, Palau A, Guzman R, Gazquez J, Arbiol J, Suo H, Puig T and Obradors X 2013 Solution-derived YBa<sub>2</sub>Cu<sub>3</sub>O<sub>7</sub> nanocomposite films with a Ba<sub>2</sub>YTaO<sub>6</sub> secondary phase for improved superconducting properties *Supercond. Sci. Technol.* **26** 015001
- [28] Engel S, Thersleff T, Huhne R, Schultz L and Holzapfel B 2007 Enhanced flux pinning in YBa<sub>2</sub>Cu<sub>3</sub>O<sub>7</sub> layers by the formation of nanosized BaHfO<sub>3</sub> precipitates using the chemical deposition method *Appl. Phys. Lett.* **90** 102505
- [29] Ye S, Suo H, Wu Z, Liu M, Xu Y, Ma L and Zhou M 2011 Preparation of solution-based YBCO films with BaSnO<sub>3</sub> particles *Physica C* **471** 265
- [30] Llordés A, Palau A, Gazquez J, Coll M, Vlad R, Pomar A, Arbiol J, Guzmán R, Ye S, Rouco V, Sandiumenge F, Ricart S, Puig T, Varela M, Chateigner D, Vanacken J, Gutierrez J, Moshchalkov V, Deutcher G, Magen C and Obradors X 2012 Nanoscale strain-induced pair suppression as a source of vortex pinning in high-temperature superconductors *Nat. Mater.* **11** 329
- [31] Coll M, Guzmán R, Gazquez J, Ye S, Puig T and Obradors X 2014 Size-controlled spontaneously segregated Ba<sub>2</sub>YTaO<sub>6</sub> nanoparticles in YBa<sub>2</sub>Cu<sub>3</sub>O<sub>7</sub> nanocomposites obtained by chemical solution deposition *Supercond. Sci. Technol.* **27** 044008
- [32] Miura M, Maiorov B, Willis J O, Kato T, Sato M, Izumi T, Shiohara Y and Civale L 2013 The effects of density and size of BaMO<sub>3</sub> (M=Zr, Nb, Sn) nanoparticles on the vortex glassy and liquid phase in (Y,Gd)Ba<sub>2</sub>Cu<sub>3</sub>O<sub>y</sub> coated conductors *Supercond. Sci. Technol.* **26** 035008
- [33] Miura M, Yoshizumi M, Izumi T and Shiohara Y 2010 Formation mechanism of BaZrO<sub>3</sub> nanoparticles in Y<sub>1-x</sub>Sm<sub>x</sub>Ba<sub>2</sub>Cu<sub>3</sub>O<sub>y</sub>-coated conductors derived from trifluoroacetate metal-organic deposition *Supercond. Sci. Technol.* **23** 014013
- [34] Deutscher G 2012 The role of Cu-O bond length fluctuations in the high temperature superconductivity mechanism *J. Appl. Phys.* **111** 112603
- [35] Bretos I, Schneller T, Falter M, Backer M, Hollmann E, Wordenweber R, Molina-Luna L, Van Tendeloo G and Eibl O 2015 Solution-derived YBa<sub>2</sub>Cu<sub>3</sub>O<sub>7-δ</sub> (YBCO) superconducting films with BaZrO<sub>3</sub> (BZO) nanodots based on reverse micelle stabilized nanoparticles *J. Mater. Chem. C* **3** 3971
- [36] Martínez-Julian F, Ricart S, Pomar A, Coll M, Abellan P, Sandiumenge F, Casanove M J, Obradors X, Puig T, Pastoriza-Santos I and Liz-Marzán L M 2011 Chemical solution approaches to YBa<sub>2</sub>Cu<sub>3</sub>O<sub>7-δ</sub>-Au nanocomposite superconducting thin films *J. Nanosci. Nanotechnol.* **11** 3245
- [37] EUROTAPES [www.eurotapes.eu](http://www.eurotapes.eu) Grant Agreement EU-FP7 NMP-LA-2012-280432
- [38] Gerbec J A, Magana D, Washington A and Strouse G F 2005 Microwave-Enhanced Reaction Rates for Nanoparticle Synthesis *J. Am. Chem. Soc.* **127** 15791

- [39] Solano E, Perez-Mirabet L, Martinez-Julian F, Guzman R, Arbiol J, Puig T, Obradors X, Yanez R, Pomar A, Ricart S and Ros J 2012 Facile and efficient one-pot solvothermal and microwave-assisted synthesis of stable colloidal solutions of  $\text{MFe}_2\text{O}_4$  spinel magnetic nanoparticles *J. Nanopart. Res.* **14** 1034
- [40] De Roo J, Justo Y, De Keukeleere K, Van den Broeck F, Martins J C, Van Driessche I and Hens Z 2015 Carboxylic-Acid-Passivated Metal Oxide Nanocrystals: Ligand Exchange Characteristics of a New Binding Motif *Angew. Chem. Int. Ed.* **54** 6488
- [41] De Keukeleere K, De Roo J, Lommens P, Martins J C, Van Der Voort P and Van Driessche I 2015 Fast and Tunable Synthesis of  $\text{ZrO}_2$  Nanocrystals: Mechanistic Insights into Precursor Dependence *Inorg. Chem.* **54** 3469
- [42] De Roo J, Van den Broeck F, De Keukeleere K, Martins J C, Van Driessche I and Hens Z 2014 Unravelling the Surface Chemistry of Metal Oxide Nanocrystals, the Role of Acids and Bases *J. Am. Chem. Soc.* **136** 9650
- [43] De Keukeleere K, Feys J, Meire M, De Roo J, De Buysser K, Lommens P and Van Driessche I 2013 Solution-based synthesis of  $\text{BaZrO}_3$  nanoparticles: conventional versus microwave synthesis *J. Nanopart. Res.* **15** 1
- [44] Deng Z-X, Wang C and Li Y-D 2002 New Hydrolytic Process for Producing Zirconium Dioxide, Tin Dioxide, and Titanium Dioxide Nanoparticles *J. Am. Ceram. Soc.* **85** 2837
- [45] Garnweitner G, Goldenberg L M, Sakhno O V, Antonietti M, Niederberger M and Stumpe J 2007 Large-Scale Synthesis of Organophilic Zirconia Nanoparticles and their Application in Organic–Inorganic Nanocomposites for Efficient Volume Holography *Small* **3** 1626
- [46] Niederberger M, Bartl M H and Stucky G D 2002 Benzyl Alcohol and Titanium Tetrachloride A Versatile Reaction System for the Nonaqueous and Low-Temperature Preparation of Crystalline and Luminescent Titania Nanoparticles *Chem. Mater.* **14** 4364
- [47] Roma N, Morlens S, Ricart S, Zalamova K, Moreto J M, Pomar A, Puig T and Obradors X 2006 Acid anhydrides: a simple route to highly pure organometallic solutions for superconducting films *Supercond. Sci. Technol.* **19** 521
- [48] Brzezińska-Miecznik J, Haberko K and Bucko M M 2002 Barium zirconate ceramic powder synthesis by the coprecipitation–calcination technique *Mater. Lett.* **56** 273
- [49] Buha J, Arcon D, Niederberger M and Djerdj I 2010 Solvothermal and surfactant-free synthesis of crystalline  $\text{Nb}_2\text{O}_5$ ,  $\text{Ta}_2\text{O}_5$ ,  $\text{HfO}_2$ , and Co-doped  $\text{HfO}_2$  nanoparticles *Phys. Chem. Chem. Phys.* **12** 15537
- [50] Hu J, Hu X, Chen A and Zhao S 2014 Directly aqueous synthesis of well-dispersed superparamagnetic  $\text{Fe}_3\text{O}_4$  nanoparticles using ionic liquid-assisted co-precipitation method *J. Alloys Compd.* **603** 1
- [51] Joo J, Yu T, Kim Y W, Park H M, Wu F, Zhang J Z and Hyeon T 2003 Multigram Scale Synthesis and Characterization of Monodisperse Tetragonal Zirconia Nanocrystals *J. Am. Chem. Soc.* **125** 6553
- [52] Park J, Joo J, Kwon S G, Jang Y and Hyeon T 2007 Synthesis of Monodisperse Spherical Nanocrystals *Angew. Chem. Int. Ed.* **46** 4630
- [53] Veith M, Mathur S, Lecerf N, Huch V, Decker T, Beck H, Eiser W and Haberkorn R 2000 Sol-Gel Synthesis of Nano-Scaled  $\text{BaTiO}_3$ ,  $\text{BaZrO}_3$  and  $\text{BaTi}_{0.5}\text{Zr}_{0.5}\text{O}_3$  Oxides via Single-Source Alkoxide Precursors and Semi-Alkoxide Routes *J. Sol-Gel Sci. Technol.* **17** 145
- [54] De Roo J, De Keukeleere K, Feys J, Lommens P, Hens Z and Van Driessche I 2013 Fast, microwave-assisted synthesis of monodisperse  $\text{HfO}_2$  nanoparticles *J. Nanopart. Res.* **15** 1
- [55] Uhlmann D R, Chalmers B and Jackson K A 1964 Interaction Between Particles and a Solid-Liquid Interface *J. Appl. Phys.* **35** 2986
- [56] Pötschke J and Rogge V 1989 On the behaviour of foreign particles at an advancing solid-liquid interface *J. Cryst. Growth* **94** 726
- [57] Shiohara Y and Endo A 1997 Crystal growth of bulk high-Tc superconducting oxide materials *Mater. Sci. Eng. R-Rep.* **19** 1

- [58] Carrillo A E, Puig T, Plain J, Figueras J and Obradors X 2000  $\text{Y}_2\text{BaCuO}_5$ -free melt textured  $\text{YBa}_2\text{Cu}_3\text{O}_7$ : a search for the reference sample *Physica C* **336** 213
- [59] Kim C-J, Kim K-B and Hong G-W 1995 Nonuniform distribution of second phase particles in melt-textured Y-Ba-Cu-O oxide with metal oxide ( $\text{CeO}_2$ ,  $\text{SnO}_2$ , and  $\text{ZrO}_2$ ) addition *J. Mater. Res.* **10** 1605
- [60] Gazquez J, Coll M, Roma N, Sandiumenge F, Puig T and Obradors X 2012 Structural defects in TFA-YBCO thin films *Supercond. Sci. Technol.* **25** 065009
- [61] Coll M, Gazquez J, Huhne R, Holzapfel B, Morilla Y, Garcia-Lopez J, Pomar A, Sandiumenge F, Puig T and Obradors X 2009 All chemical  $\text{YBa}_2\text{Cu}_3\text{O}_7$  superconducting multilayers: Critical role of  $\text{CeO}_2$  cap layer flatness *J. Mater. Res.* **24** 1446
- [62] Sánchez-Valdés C F, Puig T and Obradors X 2015 In situ study through electrical resistance of growth rate of trifluoroacetate-based solution-derived  $\text{YBa}_2\text{Cu}_3\text{O}_7$  films *Supercond. Sci. Technol.* **28** 024006
- [63] Chen H, Zalamova K, Pomar A, Granados X, Puig T and Obradors X 2010 Nucleation and growth rate influence on microstructure and critical currents of TFA- $\text{YBa}_2\text{Cu}_3\text{O}_7$  under low-pressure conditions *J. Mater. Res.* **25** 2371
- [64] Chen H, Zalamova K, Pomar A, Granados X, Puig T and Obradors X 2010 Growth rate control and solid-gas modeling of TFA- $\text{YBa}_2\text{Cu}_3\text{O}_7$  thin film processing *Supercond. Sci. Technol.* **23** 034005
- [65] Puig T, Gutierrez J, Pomar A, Llordes A, Gazquez J, Ricart S, Sandiumenge F and Obradors X 2008 Vortex pinning in chemical solution nanostructured YBCO films *Supercond. Sci. Technol.* **21** 034008
- [66] Guzman R, Gazquez J, Rouco V, Palau A, Magen C, Varela M, Arbiol J, Obradors X and Puig T 2013 Strain-driven broken twin boundary coherence in  $\text{YBa}_2\text{Cu}_3\text{O}_{7.8}$  nanocomposite thin films *Appl. Phys. Lett.* **102** 081906
- [67] Rouco V, Palau A, Guzman R, Gazquez J, Coll M, Obradors X and Puig T 2014 Role of twin boundaries on vortex pinning of CSD YBCO nanocomposites *Supercond. Sci. Technol.* **27** 125009
- [68] Blatter G, Feigel'man M V, Geshkenbein V B, Larkin A I and Vinokur V M 1994 Vortices in high-temperature superconductors *Rev. Mod. Phys.* **66** 1125
- [69] Gutierrez J, Puig T, Gibert M, Moreno C, Roma N, Pomar A and Obradors X 2009 Anisotropic c-axis pinning in interfacial self-assembled nanostructured trifluoroacetate- $\text{YBa}_2\text{Cu}_3\text{O}_{7-x}$  films *Appl. Phys. Lett.* **94** 172513
- [70] Civale L, Maiorov B, Serquis A, Willis J O, Coulter J Y, Wang H, Jia Q X, Arendt P N, MacManus-Driscoll J L, Maley M P and Foltyn S R 2004 Angular-dependent vortex pinning mechanisms in  $\text{YBa}_2\text{Cu}_3\text{O}_7$  coated conductors and thin films *Appl. Phys. Lett.* **84** 2121
- [71] Palau A, Puig T, Obradors X, Pardo E, Navau C, Sanchez A, Usoskin A, Freyhardt H C, Fernández L, Holzapfel B and Feenstra R 2004 Simultaneous inductive determination of grain and intergrain critical current densities of  $\text{YBa}_2\text{Cu}_3\text{O}_{7-x}$  coated conductors *Appl. Phys. Lett.* **84** 230
- [72] Yamada Y, Takahashi K, Kobayashi H, Konishi M, Watanabe T, Ibi A, Muroga T, Miyata S, Kato T, Hirayama T and Shiohara Y 2005 Epitaxial nanostructure and defects effective for pinning in  $\text{Y(RE)Ba}_2\text{Cu}_3\text{O}_{7-x}$  coated conductors *Appl. Phys. Lett.* **87** 132502
- [73] Samoilenkov S V, Boytsova O V, Amelichev V A and Kaul A R 2011 Anisotropic strain of  $\text{BaZrO}_3$ ,  $\text{BaCeO}_3$  and  $\text{Y}_2\text{O}_3$  nanoinclusions in a  $\text{YBa}_2\text{Cu}_3\text{O}_{7-x}$  epitaxial film matrix and its relation to the oxygen content of the superconductor *Supercond. Sci. Technol.* **24** 055003
- [74] Palau A, Llordes A, Gibert M, Puig T, Pomar A and Obradors X 2011 Pinning Landscape Analysis in YBCO Films With Epitaxial and/or Non-Coherent BZO Nanoparticles *IEEE Trans. Appl. Supercond.* **21** 3243



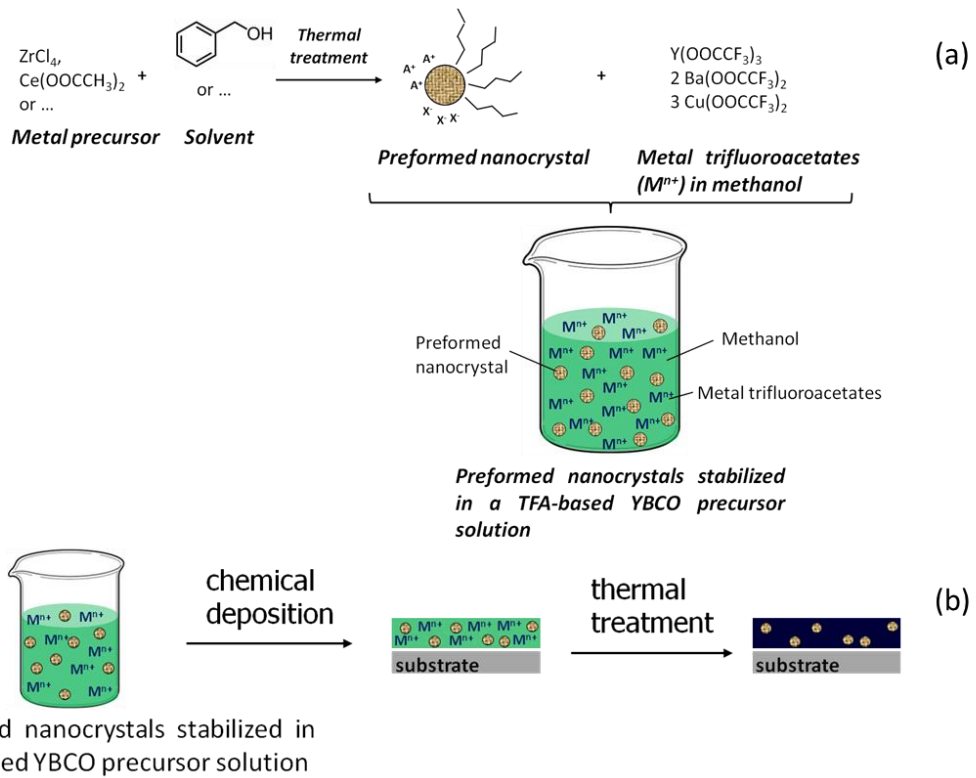


Figure 1 .- General layout of the procedure followed to prepare superconducting nanocomposites from colloidal solutions (a) Synthesis methodology of the preformed nanoparticles, stabilized sterically using long chains and/or charge stabilized, and colloidal solution preparation with the TFA precursors of the YBCO films; (b) Deposition of the colloidal solution and thermal treatments to dry the solution, to pyrolyze the metalorganic precursors and to grow the nanocomposite YBCO films.

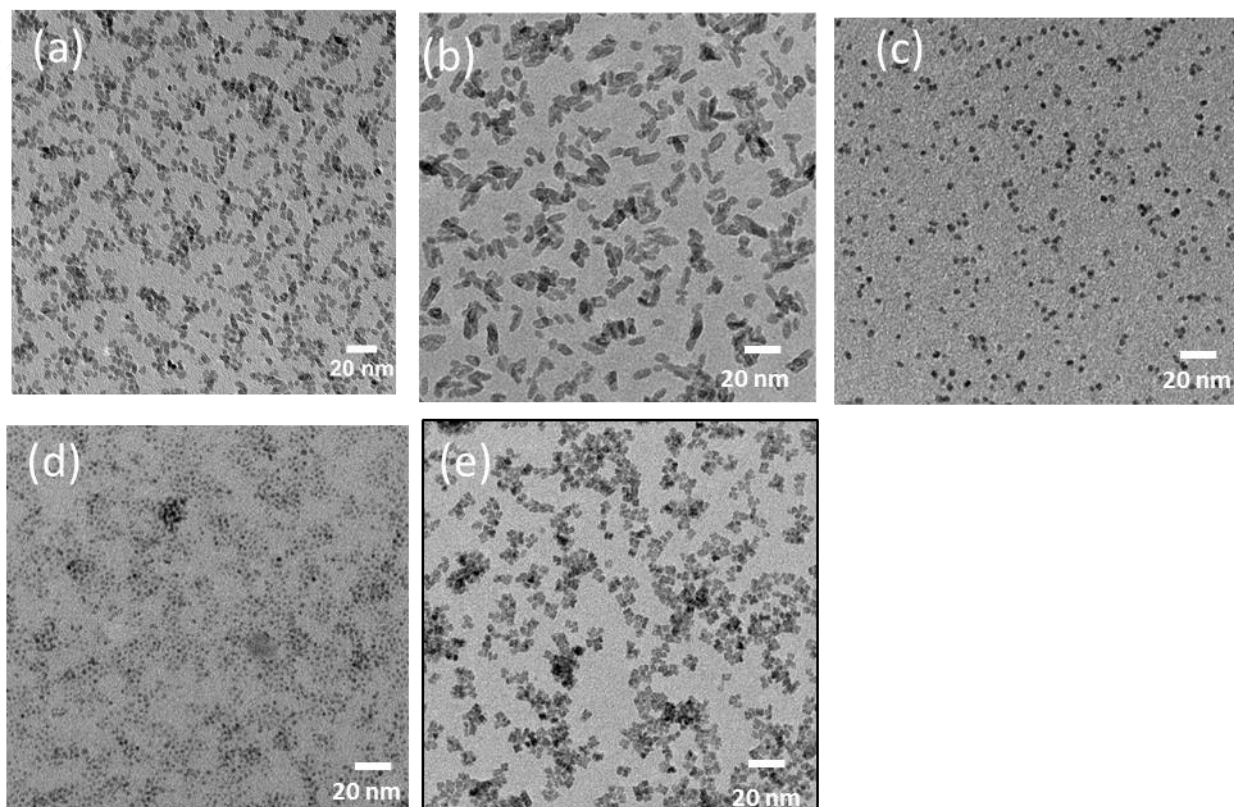


Figure 2. TEM of colloidal solutions of nanoparticles: (a)  $\text{ZrO}_2$  prepared via microwave activation and charge stabilized; (b)  $\text{ZrO}_2$  prepared via thermal activation stabilized with decanoic acid; (c)  $\text{CeO}_2$  prepared via microwave and stabilized with TREG, (d)  $\text{CeO}_2$  prepared via microwave and stabilized with decanoic acid; (e)  $\text{CeO}_2$  prepared via microwave and stabilized with  $\text{BzOH}$ .

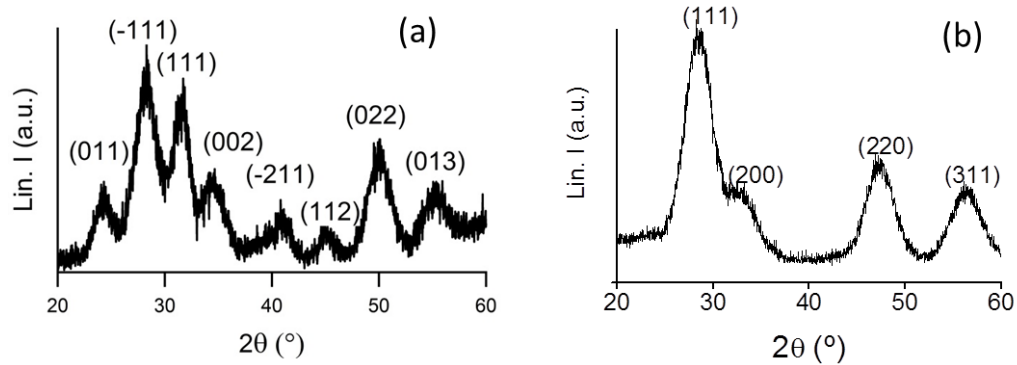


Figure 3. XRD powder patterns of nanoparticles: (a)  $ZrO_2$  obtained via microwave activation and stabilized in chloroform; (b)  $CeO_2$  stabilized with TREG.

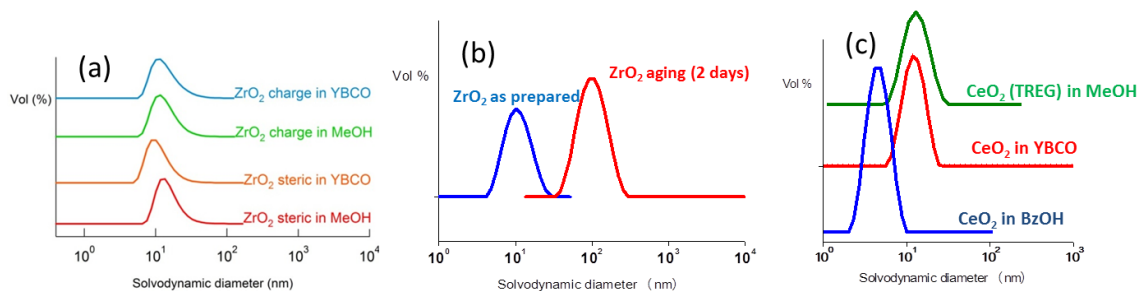


Figure 4. DLS analysis of (a)  $ZrO_2$  nanoparticles prepared by microwave activation and steric and charge stabilized in MeOH and in YBCO solution; (b) Aging of  $ZrO_2$  nanoparticles prepared by thermal activation and steric stabilized in YBCO solution; (c)  $CeO_2$  nanoparticles prepared by microwave activation, steric stabilized in MeOH, BzOH and in YBCO solution.

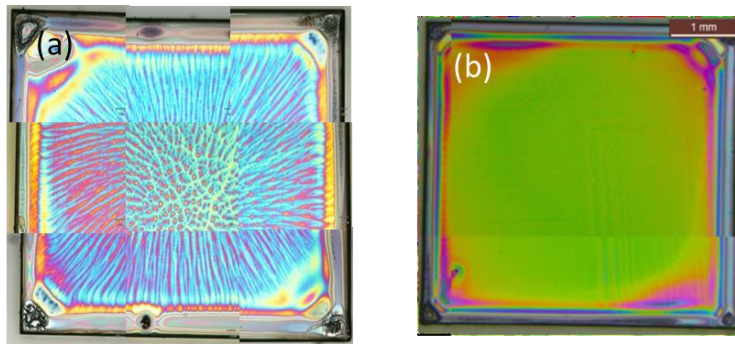


Figure 5. Optical Microscope Images of (a) Pyrolyzed ex-situ YBCO nanocomposite with  $\text{CeO}_2$ -TREG nanoparticles (b) Pyrolyzed ex-situ YBCO nanocomposite with  $\text{CeO}_2$ -decanoic acid nanoparticles

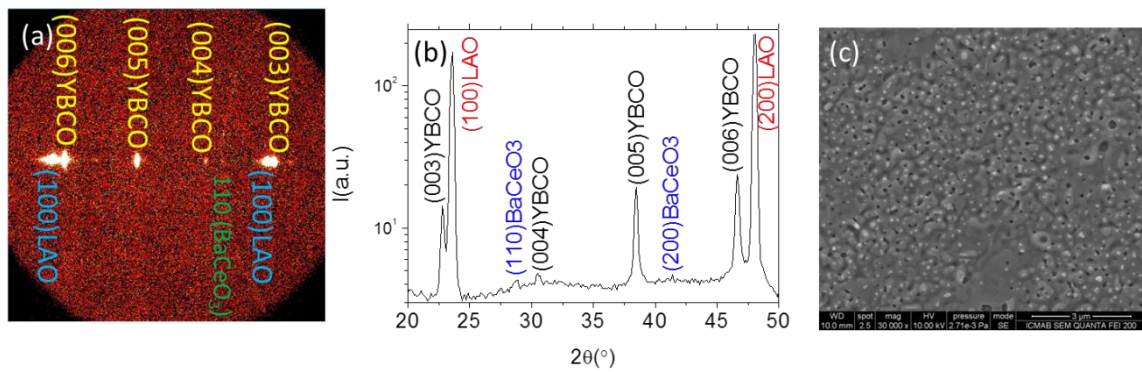


Figure 6. (a) 2D-XRD  $\theta$ - $2\theta$  pattern of a 8 mol %  $\text{CeO}_2$  YBCO nanocomposite with 2 nm  $\text{CeO}_2$  NPs; (b) Integrated spectra from (a); (c) SEM image of a 8 mol %  $\text{CeO}_2$ -YBCO nanocomposite film.

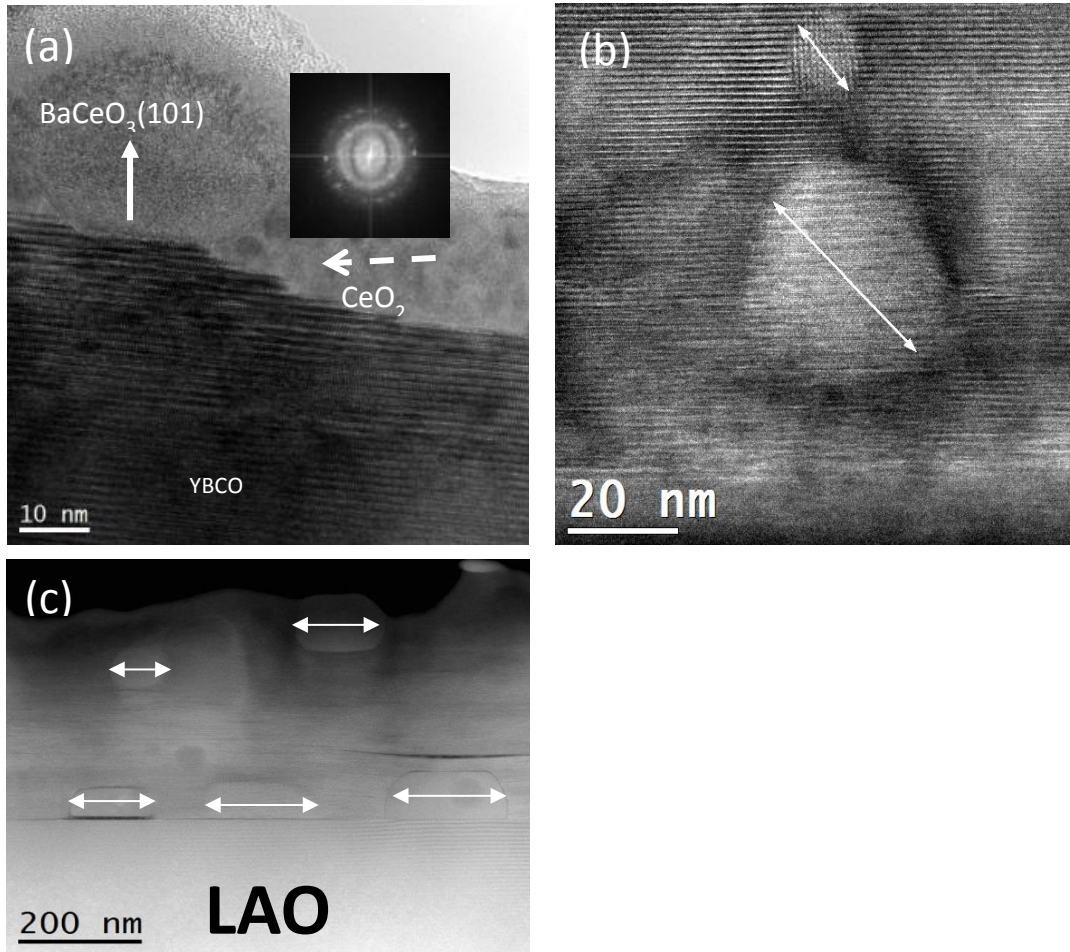


Figure 7. (a) TEM images of nanocomposites grown with 2 nm  $\text{CeO}_2$  NPs:  $\text{BaCeO}_3$  formation (white arrow) and  $\text{CeO}_2$  (dashed white arrow) NPs are detected in the surface of the film; (b) and (c) TEM images of a nanocomposite grown with 6 nm  $\text{CeO}_2$  NPs. Some of the  $\text{BaCeO}_3$  NPs (white arrows) are at the interface (epitaxial) and some are trapped in the matrix with random orientation. The YBCO matrix displays a non-negligible concentration of stacking faults.

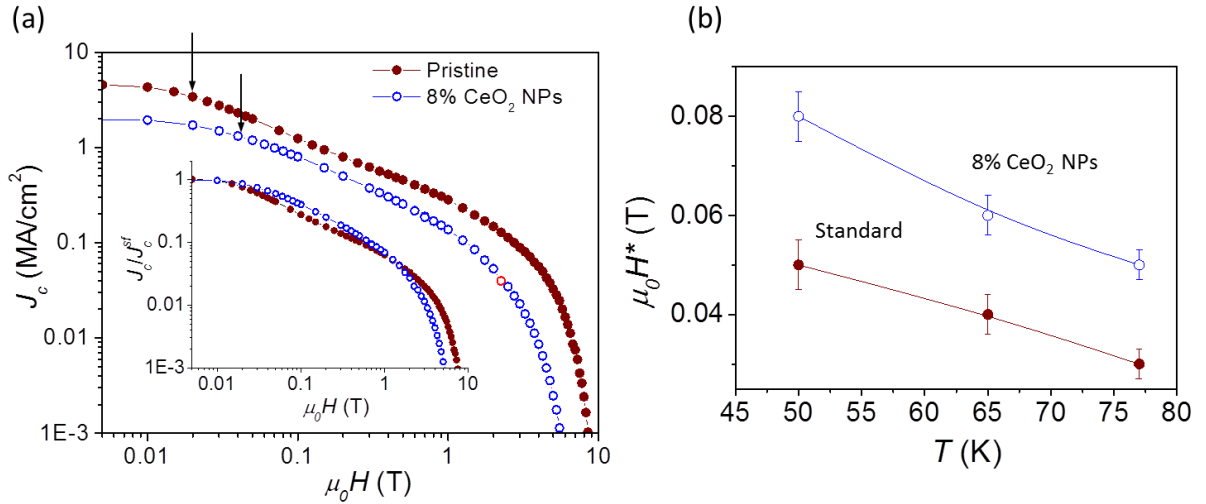


Figure 8. (a) Critical current density field dependence for a pristine YBCO sample and a film with 8 mol % CeO<sub>2</sub> NPs at 77K. Arrows depict the field at the boundary of single vortex pinning regime,  $\mu_0 H^*$ . Inset shows the same curves normalized at self-field  $J_c^{sf}$ ; (b) Temperature dependence of  $\mu_0 H^*$  for the two films.

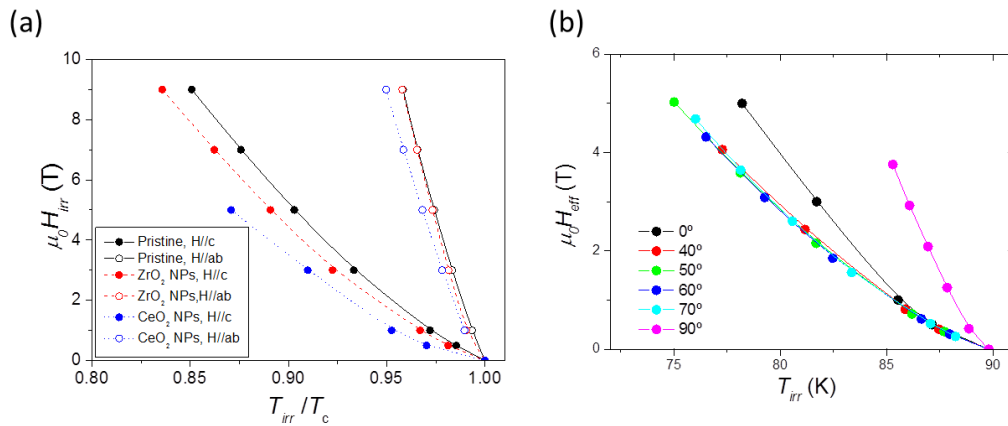


Figure 9. (a) Irreversibility lines in a reduced temperature representation for a pristine sample and nanocomposites with 8 mol % CeO<sub>2</sub> and 16 mol % ZrO<sub>2</sub> NPs, for magnetic field applied parallel to the c axis (solid dots) and to the a-b planes (empty dots); (b) Isotropic collapse of the Irreversibility line, measured at different magnetic field orientations for the CeO<sub>2</sub> nanocomposite, with  $\gamma_{eff} \sim 2.4$ .

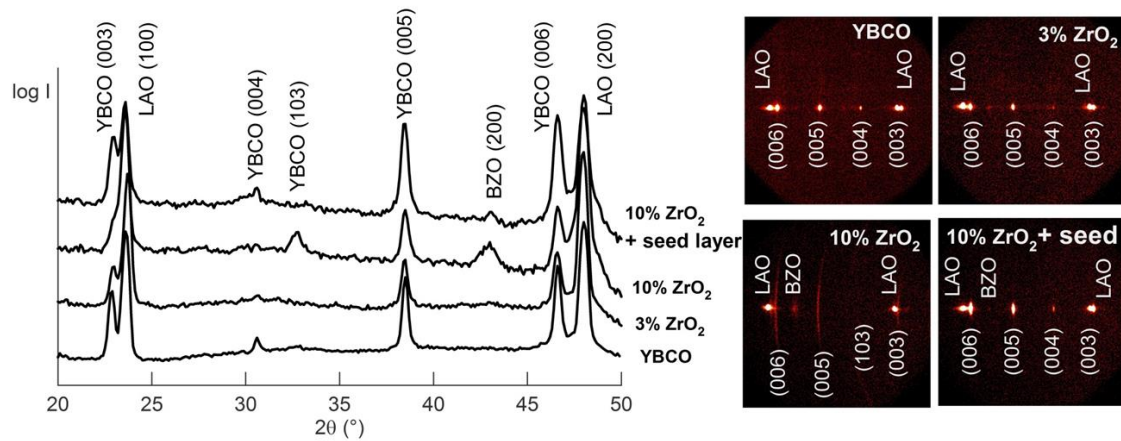


Figure 10. (a)  $\theta$ - $2\theta$  X-ray diffraction patterns of nanocomposite films with several contents of ZrO<sub>2</sub> nanoparticles prepared via microwave activation and grown on LaAlO<sub>3</sub> single crystals or in top of a YBCO seed layer; (b) Corresponding 2D X-ray diffraction patterns.

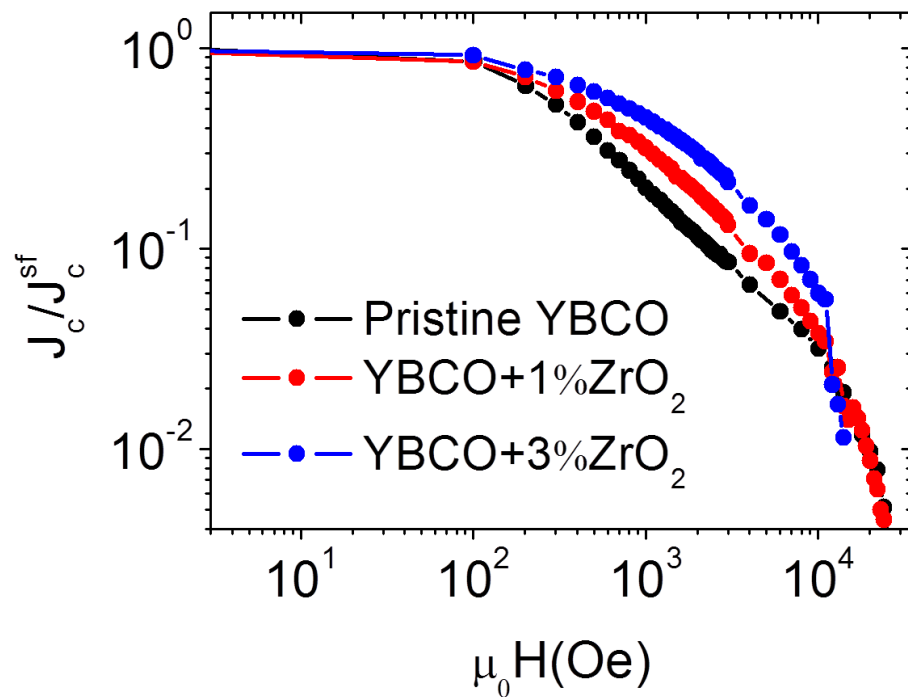


Figure 11. Magnetic field dependence of the critical current density measured with SQUID magnetometry of nanocomposites with ZrO<sub>2</sub> nanoparticles prepared via microwave activation and grown on top of LaAlO<sub>3</sub> single crystals.

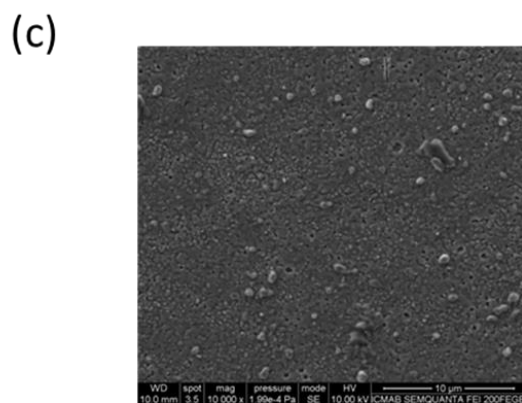
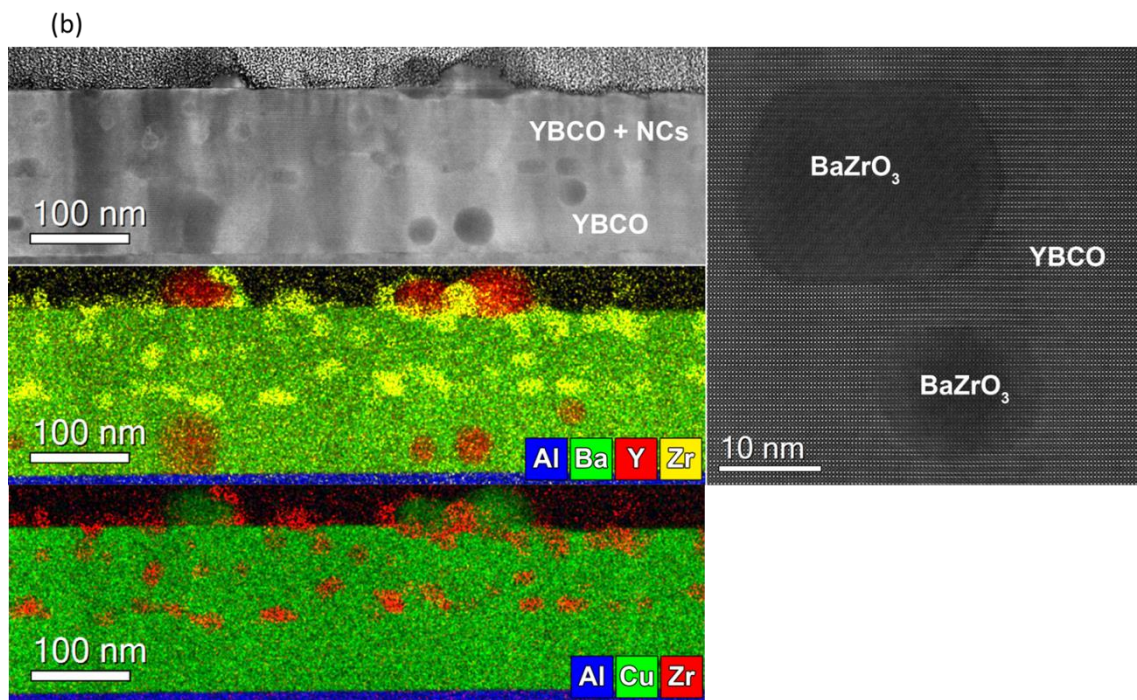
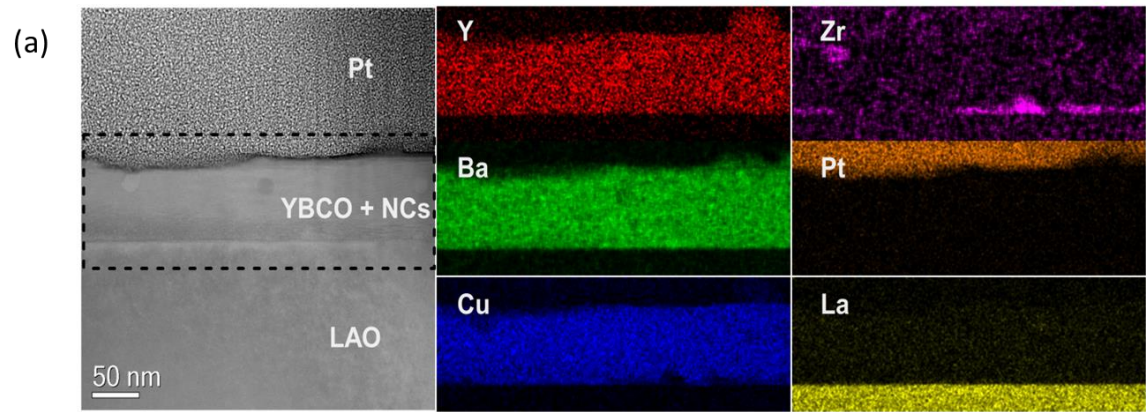


Figure 12. TEM and EDX maps of (a) YBCO nanocomposite with 3 mol %  $ZrO_2$  NPs ; (b) YBCO nanocomposite with 10 mol %  $ZrO_2$  NPs grown on top of 50 nm seed layer of YBCO ; (c) SEM picture showing the surface of the nanocomposite with 10 mol %  $ZrO_2$  NPs.

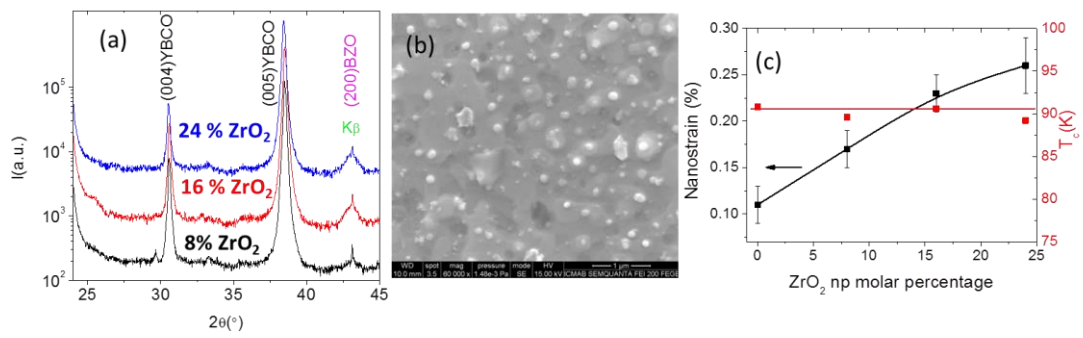


Figure 13. (a) XRD patterns of nanocomposites with 8%, 16% and 24 mol % ZrO<sub>2</sub> nanorods; (b) SEM image of a 16 mol % ZrO<sub>2</sub>-nanocomposite; (c) Value of nanostrain and critical temperature for nanocomposites with different percentage of ZrO<sub>2</sub> nanorods

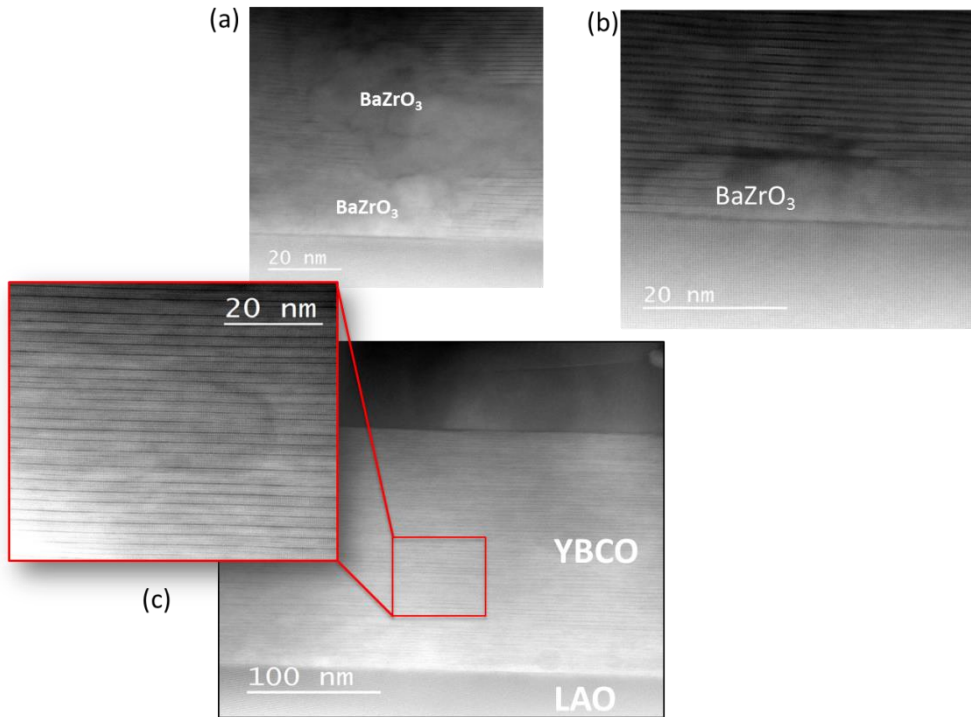


Figure 14. (a) TEM images of a nanocomposite with 16 mol %  $ZrO_2$  NPs. (a) and (b) coarsening of BZO NPs nucleating at the substrate surface; (c) Low and High resolution images of the YBCO matrix showing a high density of stacking faults.

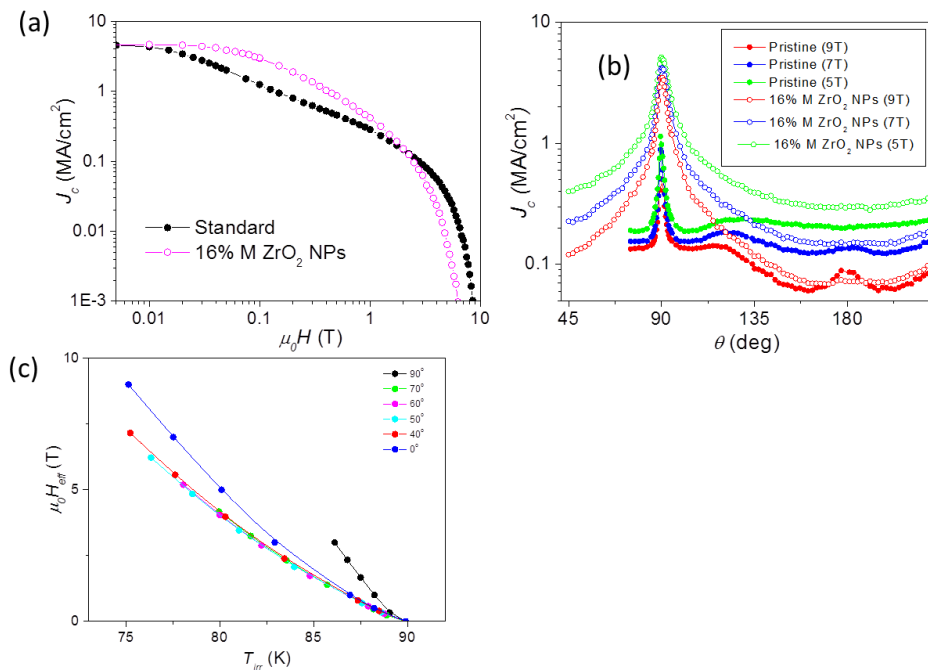


Figure 15. Superconducting properties of nanocomposite with 16 mol %  $ZrO_2$  nanorods compared with a pristine film, (a) Field dependence of the critical current density at 77K, normalized at self field; (b) Angular dependence of  $J_c$  at 65K for different applied magnetic fields in the nanocomposite as compared to pristine samples; (c) Isotropic collapse of the Irreversibility line for the nanocomposite, measured at different magnetic field orientations, with  $\gamma_{eff} \sim 3$ .

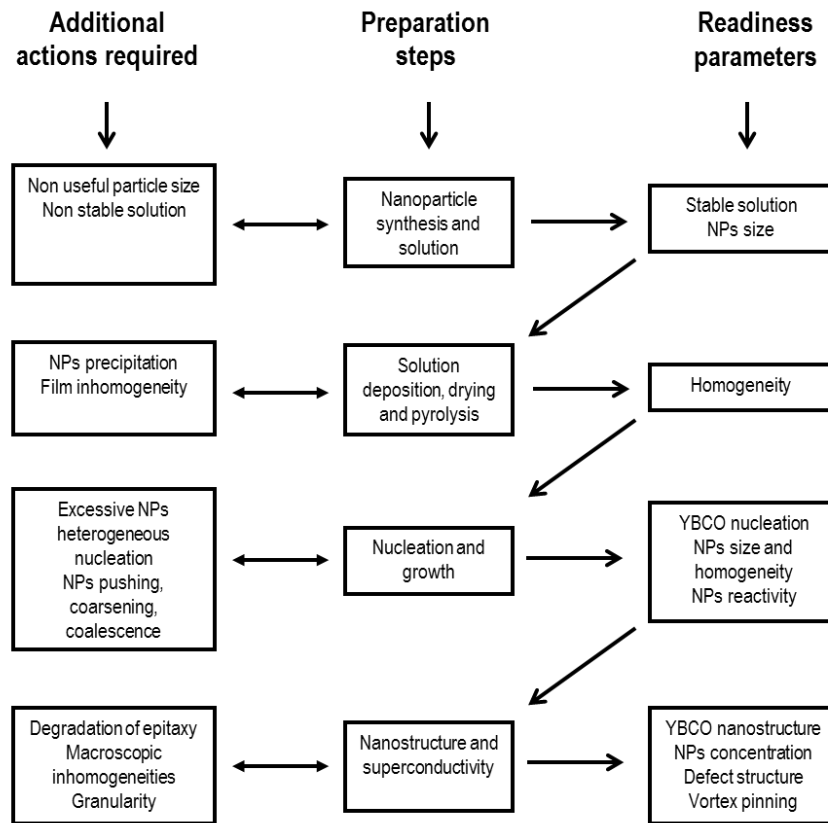


Figure 16. Sketch of the different steps involved in the CSD ex-situ nanocomposite approach.